

POLITECNICO DI TORINO

Department of Mechanical and Aerospace Engineering

Master's Degree in Aerospace Engineering



Master's Degree Thesis

Feasibility study of ESA missions with G-band radar for ice cloud observations

Supervisors

Prof. Alessandro Battaglia

Prof. Sabrina Corpino

Prof. Fabrizio Stesina

Candidate

Marco Coppola

2023/2024 Academic year

Summary

This master's thesis investigates the advantages and disadvantages of deploying a spaceborne G-Band weather radar system, with a primary focus on its potential contributions to atmospheric profiling and cloud microphysics characterization. The study proposes that G-band radar, used in conjunction with other radar systems at lower frequencies (Ka and W Bands) that have already been deployed and demonstrated in space, can offer improved microphysical retrievals of hydrometeor size, scattering properties and hydrometeor water content.

G-Band (1.5 mm wavelength) operates at higher frequency than conventional cloud radars at Ka and W bands; since atmospheric target scatter G-band radiation mainly in the non Rayleigh regime new possibilities in profiling high altitudes ice cloud, super cooled liquid water clouds and precipitating snow could be unlocked. Clouds and precipitation systems significantly impact Earth's hydrological and radiation budget and as we stand today there are no valid methods to evaluate the quantity and position of supercooled liquid water clouds, which are an important contribution to earth radiation budget. Uncertainties in their representation contribute to the largest source of uncertainty in climate sensitivity estimates, accurate estimation of cloud properties, including particle size distribution and liquid water path (LWP), is crucial for improving weather and climate models.

In this study we present simulations of a 238 GHz radar paired with a 35 GHz and a 94 GHz satellite passing over the globe in a polar orbit to survey the synergy and complementarity between the systems that could unveil regions with small water content below the actual detectable threshold thanks to a Differential Reflectivity between the frequencies.

The work in this thesis is paramount for ongoing preparatory studies that are important for the quest of demonstrating the feasibility of the technology within Earth observation space programs like the NASA Cloudcube and the ESA SCOUTS and Earth Explorer programs. The simulations are conducted in MatLab with

hydrometeor profiles derived from the Afternoon train (A-train) constellation observations and atmospheric properties from co-located ECMWF products. The study was conducted in collaboration with University of Leicester.

Results of the sensitivity and synergy-complementarity studies suggest that it would be beneficial to pair a G-Band radar with a Ka and W Band radar. In high latitudes regions and low latitudes at high altitudes regions the differences in the scattering signals measured from two different frequency radars are indicative of the characteristic dominions of the targets, whereas in low latitude regions the pair could be ineffective due to high level of water vapour absorption experienced at G-band. The increased attenuation experienced at 238 GHz improve retrievals of small/moderate liquid water content (LWC) and precipitation rate when paired with W-band or Ka-band. This is particularly noticeable in periods of low rainfall where the W-band and Ka-band radars experience little attenuation while at G-band is much greater.

Results of the supercooled liquid water cloud (SCLWC) study demonstrate that, in a multi-frequency approach, it could be possible the detection of the aforementioned clouds with increased sensitivity for larger liquid water contents, by exploiting the dual frequency differential attenuation signal.

Table of Contents

List of Tables	VII
List of Figures	VIII
Acronyms	XI
1 Radar principles and radar scattering properties	5
1.1 Radar principles	5
1.2 Hydrometeor types	7
1.3 Single particle scattering properties	7
1.4 Particle size distribution properties	11
1.4.1 Attenuation	14
1.4.2 Reflectivity	17
2 Simulator of a space borne Ka-W-G Band radar system	19
2.1 Simulator input: the CAPTIVATE database	19
2.1.1 Dataset used for scene generation	21
2.1.2 CAPTIVATE statistics of microphysical properties	22
2.2 Simulation of radar observables	24
2.3 Example of cases studies	25
2.3.1 High latitude	25
2.3.2 Mid latitude	27
2.3.3 Low latitude	28
2.3.4 Preliminary discussion on the potential of a dual frequency system including a G-band radar	29
3 Statistical analysis of single frequency sensitivity and of comple- mentarity and synergy for the Ka-G and W-G frequency pairs	31
3.1 Statistical analysis characteristics	32
3.2 Statistical sensitivity analysis of single frequency radar	32

3.3	Statistical synergy and complementary analysis of frequency pairs	
	Ka-G, W-G	34
3.4	Surface detection analysis	38
4	Super Cooled Liquid Water Cloud insertion effects to a profile retrieval	40
4.1	SCLWC insertion in south Atlantic system	41
5	Conclusions	44
	Bibliography	47

List of Tables

2.1	Past and future missions frequency divided sensitivity comparison with this study sensitivities choice	24
3.1	Table of radar products grid number of points and value range . . .	32

List of Figures

1.1	Scattering regimes visible in a σ_b - diameter logarithmic plot for rain particles at 283K. Rayleigh regime linear behaviour is visible for diameters lower than wavelength and Mie notches at diameters comparable with wavelength	8
1.2	Scattering regimes visible in a σ_b - diameter plot for various particles at 283K Ice (top left), Hail (top right), Graupel (bottom left) and Snow (bottom right); clear differences in behavior appears in non Rayleigh regime.	9
1.3	Rain extinction per unit mass at different frequencies: Ka (red), W (blue) and G (magenta); Peak extinction occurs at decreasing diameters with increasing frequency.	11
1.4	Ice (top left), Hail (top right) and Graupel (bottom) $\frac{\sigma_{ext}}{m}$ -D at different frequencies: Ka (red), W (blue) and G (magenta); Oscillating behaviour can be distinguished from rain smoother behaviour.	12
1.5	Rain extinction coefficient per unit mass at different frequencies: Ka (red), W (blue) and G (magenta) and different μ depicted with different lines; Peak attenuation occurs at decreasing diameters with increasing frequency.	14
1.6	Ice (top l), Hail (top r), Graupel (bottom l) and Snow (bottom r) $\frac{K_{ext}}{m}$ - D_m at different frequencies: Ka (red), W (blue) and G (magenta) and different μ depicted with different lines; Plateaus can be spotted in ice and snow attenuation.	15
1.7	Differential attenuation Ka-G (red), W-G (blue): Rain (top c), Ice (top l), Hail (top r), Graupel (bottom l) and Snow (bottom r) at different μ depicted with different lines	16
1.8	Dual frequency ratio per unit mass Ka-G (red), W-G (blue): Rain (top c), Ice (top l), Hail (top r), Graupel (bottom l) and Snow (bottom r) at different μ depicted with different lines	18
2.1	Simulator flow chart	20

2.2	CloudSat passes over latitude (left) and sample Orbit on Feb. 15 2008 (right)	21
2.3	Annual data distribution in linear days from first January showing a lack of data in summer and fall	22
2.4	Water content of all hydrometeors profile of a full orbit (left), characteristic diameter of rain (right) black and red line represent 0°C iso-thermal	22
2.5	Two-dimensional normalized frequency of occurrence as a function of latitude band for (a)–(c) $\log(N_w) \sim D_0$ and (d)–(f) LWC–D0 of (Dolan et al. 2018) paper	23
2.6	Two-dimensional normalized frequency of occurrence as a function of latitude band for (a)–(c) $\log(N_w) \sim D_0$ and (d)–(f) LWC–D0 replica.	24
2.7	SCOUT G-band radar characteristics (top panel) and Earth Explorer (bottom panel) G-band (second and third columns) and Ka band (fourth and fifth columns) radar characteristics.	25
2.8	High latitude case study: Water content (top l) Reflectivity in Ka (top r), W (bottom l) and G (bottom r) profiles of an event of icy precipitation on February 15th 2008 over Arctic circle and Svalbard islands. Pay attention that plot color scales differs from one another	26
2.9	Mid latitude case study: Water content (top l) Reflectivity in Ka (top r), W (bottom l) and G (bottom r) of a mixed phase cloud system with liquid precipitation on 2nd January 2007 over Atlantic ocean west of Washington state. Pay attention that plot color scales differs from one another.	27
2.10	Low latitude case study: Water content (top l) Reflectivity in Ka (top r), W (bottom l) and G (bottom r) on January 3rd 2007 over central Africa. Pay attention that plot color scales differs from one another.	28
2.11	DFR of previous case studies: Ka-G (left column) W-G (right column), high latitude (top row), mid latitude (mid row r) low latitude (bottom row). Pay attention that plot color scales differs from one another	30
3.1	Statistical detection percentage in a zonal plot of G band radar at -20dBZ (first row, left panel) and -40dBZ (first row, right panel). W band at -10dBZ (second row, left panel) and -30dBZ (second row, right panel) and Ka band at 10dBZ (third row, left panel) and -20dBZ (third row, right panel). Pay attention that plot color scales differs from one another	33

3.2	W-G DFR distribution at latitude 0° and altitude 2km, red bounds represent optimal synergy bounds and light blue region represent optimal synergy region.	35
3.3	Ka-G DFR distribution at latitude -52° and altitude 9km (left) latitude -52° and altitude 9km (right), red bounds represent optimal synergy bounds and light blue region represent optimal synergy region.	35
3.4	Statistical synergy detection percentage in a zonal plot of Ka-G (top left) with -20dBZ and -40dBZ sensitivity threshold and W-G (bottom left) with -30dBZ and -20dBZ sensitivity threshold. On the right the optimal synergy percentage of DFR. Red squares represent the sampled region for Figs. 3.2-3.3. The percentage is the ratio of the blue region and the total area times 100 in figure Fig. 3.2. Notice that plot color scales differ in the different panels.	36
3.5	Statistical complementary detection percentage in a zonal plot of G-Ka (top left) with -20dBZ and -40dBZ sensitivity threshold and G-W (bottom left) with -30dBZ and -20dBZ sensitivity threshold synergy. On the right column the counterparts of complementarity: Ka-G (top left) and W-G (bottom right). First one in the frequency pair detect and the other don't. Notice that color scales differ from panel to panel.	37
3.6	Ka-band (top left), W-band (top right) and G-band (bottom) surface detection. Lower frequencies (Ka and W) experience low levels of attenuation, hence sensitivity thresholds does not affect surface detection.	39
3.7	Surface detection complementarity Ka-G with different Ka thresholds 10dBZ(left) and -20dBZ (right) surface detection and different G-band thresholds 0dBZ (magenta) -20dBZ (blue) -40dBZ (red). Same levels are reached by all the different Ka-band sensitivity thresholds.	39
4.1	Example of two SCLWC insertion in an Atlantic system	40
4.2	Atlantic system Ice water content (left) and Temperature (right). Red dotted lines indicate one of the bounds where the clouds were inserted	41
4.3	Atlantic system DFR Ka-G(left) and W-G (right). Pay attention at the different color scales	41
4.4	Atlantic system differential reflectivity (post insertion minus pre insertion) Ka-G (left) and W-G (right). Red dotted lines indicate one of the bounds where the clouds were inserted. Pay attention that color scales differs from one another.	42
4.5	Atlantic system profile at coordinates (-47° ; -49°) 2 way G-band attenuation Original (left) and SCLWC inserted (right).	43

Acronyms

CALIOP

Cloud–Aerosol Lidar and Orthogonal Polarization

CAPLIPSO

Cloud–Aerosol Lidar and Infrared Pathfinder Satellite Observation

CAPTIVATE

Cloud, Aerosol and Precipitation from mulTiple Instruments using a VARia-tional TEchnique

CPR

Cloud Profiling Radar

DFR

Differential Frequency Ratio

EarthCARE

Earth Cloud Aerosol and Radiation Explorer

ECMWF

European Centre for Medium-Range Weather Forecasts

ESA

European Space Agency

GPM

Global Precipitation Measurement

IPCC

Intergovernmental Panel on Climate Change

IWC

Ice Water Content

LUT

Lookup Table

LWC

Liquid Water Content

LWP

Liquid Water Path

MDS

Minimum Detectable Signal

MODIS

Moderate Resolution Imaging Spectroradiometer

NASA

National Aeronautics and Space Administration

PIA

Path Integrated Attenuation

SCLWC

Super Cooled Liquid Water Clouds

TRL

Technology Readiness Level

WC

Water Content

WP

Water Path

Introduction

Spaceborne radar technology represents a groundbreaking avenue for gaining a comprehensive understanding of Earth's hydrological cycle, particularly within the atmosphere. These radars, both currently operational and in the planning stages, give invaluable insights into cloud and precipitation dynamics across land and oceans, including remote and inaccessible regions. Those dynamics significantly impact Earth's hydrological and radiation budget; in addition three (out of seven) of the grand challenges posed by the World Climate Research Program [*WCRP Grand Challenges* 2022; *Climate Change* 2023] are centered on this theme: (1) Clouds, Circulation and Climate Sensitivity, (2) Understanding and Predicting Weather and Climate Extremes, and (3) Water for the Food Baskets of the World. These challenges require improving our skill in observing and predicting the locations, the time and the phenomena that leads to clouds formation, whether they precipitate or not, and, how much water content they generate in the current climate and how this might evolve in a warming climate [e.g. Alessandro Battaglia et al. 2020].

Ice clouds with possible formation of snowfall and boundary layer clouds are of particular interest for Earth radiation budget. High altitude cirrus clouds significantly influences the Earth's radiative equilibrium within the broader context of global climate dynamics while thin cirrus clouds might lead to overall warming by absorbing terrestrial thermal radiation, their thicker counterparts could induce cooling by reflecting solar radiation. Hence, accurate modeling of cirrus clouds necessitates a precise comprehension of ice microphysical processes which entails the characterization of microphysical properties like ice water content (IWC), mean characteristic size and particle concentration. High latitude/altitude precipitation occurs in the form of snowfall; it is very important for understanding ice sheet mass balance and for water management in mountainous areas. Generally profiling snow is challenging both from ground-based and from space-borne radar systems [Szyrmer et al. 2012; Skofronick-Jackson et al. 2013].

Furthermore, supercooled clouds are generally ubiquitous in ice clouds. As we stand today there are no valid methods to evaluate the amount and position of supercooled liquid water clouds, which are an important contribution to earth

radiation budget and latent heat profiles. Uncertainties in their representation contribute to the largest source of uncertainty in climate sensitivity estimates. Accurate estimation of cloud properties, including particle size distribution and liquid water path (LWP), is crucial for improving weather and climate models.

Low level and boundary-layer clouds (e.g. cumulus, stratocumulus, and stratus) play a pivotal role in facilitating the exchange of heat, water, momentum, and chemical elements between the Earth's surface and the atmosphere. Cumulus clouds typically manifest during fair weather conditions over both land and sea, while layers of stratocumulus and stratus are prevalent in subsidence regions like the anticyclonic zones in the eastern portions of subtropical oceans or polar areas. They exhibit strong reflectivity of solar radiation, thereby they play a critical role in the climate system. Moreover, they emit marginally less infrared radiation to space compared to the slightly warmer surface, resulting in a net cooling effect on climate. Consequently, even minor alterations in the distribution or characteristics of low clouds, such as changes in aerosol concentration, could either mitigate or exacerbate global warming, [Christensen et al. 2013, Liu et al. 2018].

Early endeavors for the microphysical characterization of the aforementioned cloud types concentrated on centimeter-wavelength radar development (3–10 cm), X,C and S-band, enabling extensive precipitation coverage with minimal attenuation. Subsequent theoretical and experimental undertakings have converted various radar signal properties (amplitude, phase, polarization) offering insights into precipitation particle characteristics such as size, shape, motion, and thermodynamic phase.

The 1970s and 1980s witnessed a shift toward millimeter-wavelength radar research (8.6 and 3.2 mm) from W to K-band, also called "cloud radars"; the sensitivity of these radars to cloud droplets and small ice crystals arises from their short wavelength and from the fact that in the Rayleigh scattering regime the hydrometeor cross section depends on the inverse of fourth power of the wavelength ($1/\lambda^4$). The deployment of millimeter-wavelength radars, alongside lidar systems, now constitutes a cornerstone in cloud studies [P. Kollias et al. 2007]. The studied frequency bands in this thesis are Ka (35 GHz), W (94 GHz) and G (238 GHz); Ka means above K-band, typically from 18 to 27 GHz and is also called centimeter-wavelength radar; W band has wavelength that stands in the middle between Ka and G-band. G-band is called a millimeter-wavelength radar and with all the previous frequencies stands in the microwave portion of the light spectrum.

The launch of the CloudSat Cloud Profiling Radar (CPR) mission in 2006 marked an important moment in the scientific community, featuring a pioneering 94 GHz radar in space (G. L. Stephens et al. 2002). The CPR's launch marked a paradigm shift, enabling the comprehensive observation of both clouds and associated precipitation (G. Stephens, D. Winker, et al. 2018). It transcended the conventional distinction between "precipitation" and "cloud" radars, enabling water and energy budget models validation with its broad dataset gathered over

the years.

Space-borne radars are pillars of the current global cloud and precipitation observing system. To date there are no fully functioning spaceborne cloud radar with the characteristics mentioned above, but the Global Precipitation Measurement (GPM) DPR with its low sensitivity Ka radar which focuses primarily on light to moderate rain over tropical and subtropical oceans. The CloudSat CPR [Tanelli, Durden, et al. 2008], part of the NASA A-Train constellation [D. M. Winker et al. 2009], terminated its life in Dec. 2023. It is worth mentioning the ESA commitment on the subject with its current planned mission EarthCARE (Earth Cloud Aerosol and Radiation Explorer, Illingworth et al. 2015) ready to launch in May 2024 with the objective to study the relationship of clouds, aerosols and radiation. The scientific community is eagerly planning for the next generation of spaceborne radars by identifying sciences gaps (K. Lamer et al. 2020; A. Battaglia, P. Kollias, et al. 2020; Pavlos Kollias et al. 2022) and new technologies capable of filling such gaps (Tanelli, Haddad, et al. 2018; G. Stephens, Freeman, et al. 2020); this thesis aims to help in this effort.

State of the art methods for retrieving rain microphysics utilize radar frequencies in the X, Ka and W [Frédéric Tridon, Alessandro Battaglia, and Pavlos Kollias 2013; F. Tridon and A. Battaglia 2015; Frederic Tridon et al. 2017; F. Tridon, A. Battaglia, Luke, et al. 2017; A. Battaglia, Tanelli, et al. 2020], which prove effective under various atmospheric conditions, particularly for precipitation exceeding 0.5 mm in size. X, Ka, and W-band radars may detect small cloud droplets and drizzle raindrops but they can all be considered as Rayleigh targets at these frequencies [F. Tridon, A. Battaglia, and S. Kneifel 2020]; therefore, these pairings fail to generate differential scattering signals for hydrometeors smaller than 0.5 mm and no size information can be discerned through multi-frequency techniques, even if the upper frequency is at W band. Similar conclusions are drawn when considering multi-frequency observations of ice clouds when adopting the current set of available bands [Stefan Kneifel et al. 2015; S. Kneifel et al. 2016; Frédéric Tridon, Alessandro Battaglia, Chase, et al. 2019; Mroz et al. 2021; Nguyen et al. 2022; F. Tridon, Silber, et al. 2022].

To address these constraints, researchers have pushed the development of radars operating at higher frequencies within the G-band (110 – 300 GHz) [A. Battaglia, C. D. Westbrook, et al. 2014] and over the past decade, advancements in Schottky-diode technology, frequency-multiplication-based sources, and frequency-modulated, continuous-wave radars led G-band radar systems to higher Technology Readiness Levels (TRLs), enhancing power and sensitivity to levels that meet the requirements to address the challenges. Ground based radars in the G-band, built both in the US and in the UK, and deployed in field campaigns [Katia Lamer et al. 2020; Benjamin M. Courtier et al. 2022; B. M. Courtier et al. 2024; Socuellamos et al.

2024] confirm that such instruments provide sensitivity performance as good as radars in Ka and W bands.

Furthermore, the adoption of a Ka-G frequency pair promises enhanced differential signals, bringing higher noise resilience and precision in hydrometeor mass and size retrievals. This progression underscores a concerted effort within the scientific community to augment our understanding of microphysical properties associated with drizzle and small ice particles.

This work aim to simulate a spaceborne satellite in polar orbit equipped with Ka, W and G band radar using Cloud-Sat and A-train data from 2007 to 2008 to unveil the potential of multi-frequency radar system through a statistical analysis of a collection of annual orbits conducted in MatLab. These satellites are suitable for this analysis having surveyed the globe for decades in polar sun-synchronous orbit (local time 2AM) and having produced observations of rain, ice, and cloud profiles retrieved via the CAPTIVATE algorithm [Mason et al. 2022], so they are ideal to give an ample and varied set of data through different surface, temperature, season and weather conditions. In addition ECMWF data are used as input for temperature, pressure and relative humidity, thus allowing the computation of gas attenuation.

This work is divided in five chapters. In the first one it will be presented the physics behind radar products retrieval, in particular reflectivity and attenuation; the second chapter illustrates case studies of particular interest in showing G-band capabilities and peculiarities; a statistical analysis of what a G-band radar would see in a polar orbit within a year at different latitudes and altitudes as a function of radar sensitivity will be presented in chapter three with a synergy and complementary study of multi-frequency system approach with frequency pairs (Ka-G, W-G); in chapter four will be analyzed the effects of a SCLWC inserted in a scene. Conclusions and future work are drawn in chapter five.

Chapter 1

Radar principles and radar scattering properties

To better comprehend the nature of the proposed solution it is best to explain the underlying physics of radars, the scattering regimes in which the three frequencies (Ka 35GHz, W 94GHz, G 238 GHz) work.

1.1 Radar principles

The equation relevant for the remote sensing of cloud and precipitation is the Radar equation for distributed targets. It describes the received power by an antenna in function of:

- radar parameters such as P_t : transmitted power, D_a , the diameter of the dish (assumed circular), λ : the wavelength and τ , the pulse duration;
- the transmittance of the atmosphere along the path between the target and the radar and the range, r , of the target;
- the target properties contained in Z .

$$P_r = \underbrace{\frac{1.22^2 0.55^2 10^{-18} \pi^7 c \|K_w\|^2}{1024 \log_e(2)}}_{\text{Constants}} \underbrace{\frac{P_t \tau D_a^2}{\lambda^4}}_{\text{Radar parameters}} \underbrace{\frac{T(0, r)^2}{r^2}}_{\text{Path}} \underbrace{Z}_{\text{Target properties}} \quad (1.1)$$

with the convention of using $\|K_w\|^2$ the dielectric constant of water at 283 K equal to 0.93. In Rayleigh regime:

$$Z = \int_0^\infty N(D)D^6 dD \quad (1.2)$$

N being the particle distribution and D the Diameter. Radar reflectivity is defined as follows:

$$\eta = \int_0^\infty \sigma_b N(D) dD = \frac{\pi^5 \|K\|^2}{\lambda^4} Z \quad (1.3)$$

Z is usually measured in mm^6/m^3 and it spans over a wide range of values so it is useful to introduce the quantity dBZ:

$$dBZ = 10 \log_{10}(Z) \quad (1.4)$$

Measured and effective reflectivity differ from each other, the first one is lower due to the attenuation of the radar electromagnetic wave caused by gases and hydrometeors in the path between the radar and atmospheric targets. Because the EM wave travels two-way forward and backward the total attenuation corresponds to twice the optical thickness obtained by integrating from the radar position to the range r the profile of the extinction coefficient, defined as:

$$k_e(r) = \int_0^\infty \sigma_e(D)N(D)dD \quad (1.5)$$

where $\sigma_e(D)$ is the extinction cross section. The two are related by the following equation:

$$\underbrace{Z_m(f, r)}_{[dBZ]} = \underbrace{Z_e(f, r)}_{[dBZ]} - \text{Two way attenuation} \quad (1.6)$$

Two way attenuation is also called two way Path Integrated Attenuation (PIA). Another important parameter is the Radar sensitivity and is the minimum theoretical signal that is possible to discern in an environment that has natural background noise and other noise sources like interfering signal sources (may be ground or sea returns), meteorological clutter returns, atmospheric reflections. Making the hypothesis of detecting the background noise without emitting any pulse the radar equation (1.1) could be summarized as follows:

$$P_{noise} = Const \cdot \frac{Z}{r^2} \quad (1.7)$$

and inverting the equation is possible to get the MDS:

$$Z_{min} = \frac{P_{noise}}{r^2} \cdot Const \quad (1.8)$$

where Const results from all of the radar parameters and constants. From this concept a major advantage of G band over lower frequencies can be noticed, Z_{noise} is dependant on λ^4 , the fourth power of the wavelength if considering same target, radar properties and parameters. This means that G-band over W-band has an advantage of 16dB due to the nature of the radar equation Eq. 1.1:

$$10 \log_{10} \left(\frac{238}{94} \right)^4 = 16 \text{ dB} \quad (1.9)$$

There is a caveat in this hypothesis, G-band due to technological limitations could not achieve the same levels of transmitted power of lower frequencies, but thanks to the difference in power coefficients of λ and P_t just using more power will not generate as much difference.

1.2 Hydrometeor types

Hydrometeors are classified in liquid or solid water particles formed and remaining suspended in the air:

- Cloud: smaller droplets of water that have negligible sedimentation velocity are considered cloud particles, typically with diameter below 0.2mm.
- Liquid precipitation: liquid water particles of the size between 0.2-8 mm are considered rain particles, in between cloud and rain there is drizzle that has a non-zero sedimentation velocity but is smaller than rainfall.
- Freezing precipitation: There are many types of frozen hydrometeors, snow and hail has characteristic dimension between 1–10 mm; graupel, typically under 4mm is the result of SCLWC coming in contact with snow and plate-shaped or needle particles (<1 mm) that forms icy precipitation.
- Super cooled liquid water clouds refers to liquid cloud droplets below 0°C

1.3 Single particle scattering properties

The comprehension of radar products start with single particle scattering properties, that provide clear guidelines on signal attenuation and scattering back to the receiver divided into hydrometeors contributes; once correctly simulated it can be exploited to study the behaviour of a population of hydrometeors. One of the main parameters is the Back scattering cross section (σ_b), it is the responsible of the reflectivity behaviour therefore of the radar reflectivity:

Diving deep in the single particle scattering behaviour of hydrometeors is possible to distinguish three main regions: Rayleigh, Mie and Optical or Geometrical.

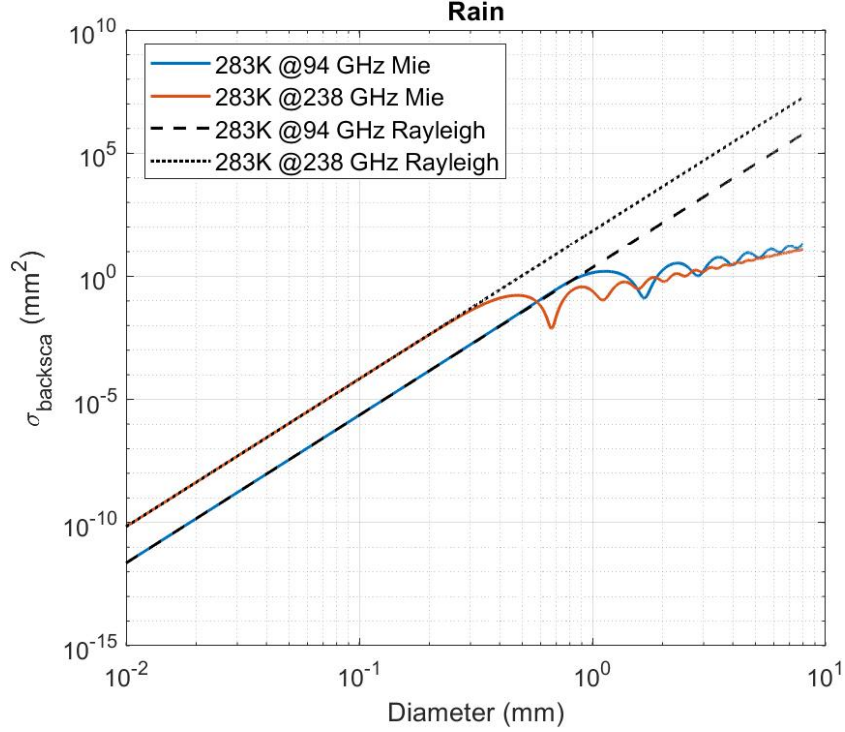


Figure 1.1: Scattering regimes visible in a σ_b - diameter logarithmic plot for rain particles at 283K. Rayleigh regime linear behaviour is visible for diameters lower than wavelength and Mie notches at diameters comparable with wavelength

The Rayleigh regime is characterized by hydrometeors much smaller than the incident wavelength (in fig. Fig. 1.1 where the curve is linear up to 0.3 mm for a rain particle detected with G band) indicating that back scattering cross-section (σ_{back}) is linear with the dimension of the scatterer and is proportional to the sixth power of the diameter and to the fourth power of the frequency [Extinction 1983].

$$\sigma_b = \frac{\pi^5 D^6}{\lambda^4 |K|^2} \quad (1.10)$$

with λ : wavelength, D :Diameter, K : Dielectric factor that is tied to the complex index of refraction $m = n' + in''$

$$|K|^2 = \left| \frac{n_w^2 - 1}{n_w^2 + 2} \right|^2 \quad (1.11)$$

It is clear that radar operating at lower wavelength take advantage of a higher back scattering cross section, resulting in better detecting small particles.

In Mie scattering regime, i.e. when the raindrop size becomes comparable or larger than the wavelength (in figure Fig. 1.1 for diameters from 0.3 mm to 2 mm), the back scattering cross section oscillates with consecutive maxima and minima with increasing particle size [Lhermitte 1990]. It is thanks to this differential behaviour between the frequencies that is possible to better detect smaller particles, in the next chapters it will be explained in further details.

The optical regime is not applicable for rain since it concern particles over 10 mm in diameter.

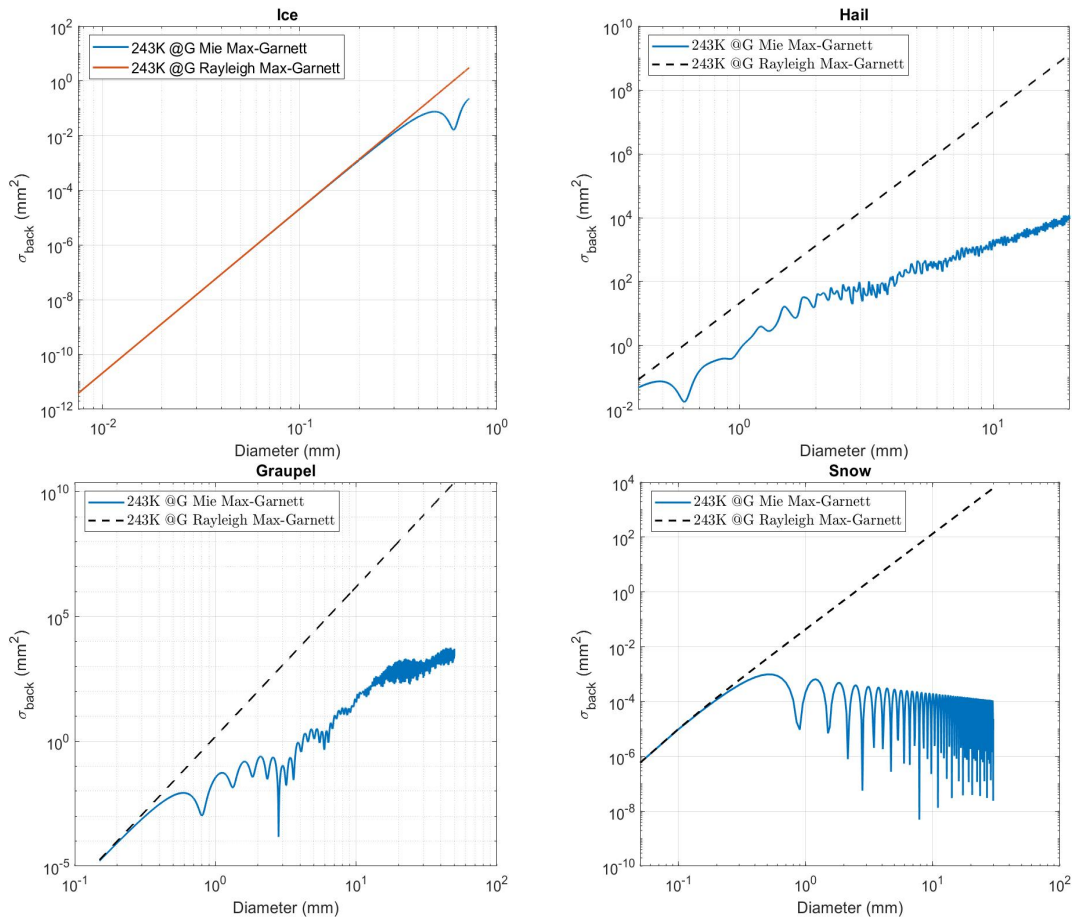


Figure 1.2: Scattering regimes visible in a σ_b - diameter plot for various particles at 283K Ice (top left), Hail (top right), Graupel (bottom left) and Snow (bottom right); clear differences in behavior appears in non Rayleigh regime.

In figure Fig. 1.2 it's represented the scattering behaviour of other important hydrometeors, Ice, Snow, Hail and Graupel.

As it can be seen all hydrometeors but ice differ strongly from Rayleigh approximation, it means that for ice is difficult to gain knowledge on the particle size based on the differential between backscattering cross sections when it's Rayleigh scatterers and Non-Rayleigh scatterers. For the computation it was used Maxwell Garnett approximation, an Effective Medium Approximation (EMA) to obtain optical properties and porosity of pure and ice mixtures, in which the effective medium (ice) consists of a matrix medium (ice) with inclusions (air).

The other important parameter that characterize the difference between G-Band and lower frequencies is the extinction cross section also called attenuation cross section. Attenuation is comprised of Absorption and Scattering, as it can be seen from equation Eq. 1.12 higher frequency as well as bigger particles determine higher attenuation, also there is a small dependence of the imaginary part of K that depends on the material of the particle.

$$\sigma_{ext} = \frac{\pi^2 D^3 \Im(-K)}{\lambda} \quad (1.12)$$

Every graph produced from now on in this chapter has analysis based on these temperatures: $T_{rain} = 283K$, $T_{ice} = T_{hail} = T_{graupel} = T_{snow} = 253K$. At high frequencies as for G-band absorption derive mainly from water vapour as shown in figure Fig. 1.3[Alessandro Battaglia et al. 2020] and depends on particle mass so it is useful to plot the extinction per unit mass to give a true measure of the contribution of different size particles.

$$\text{Ext. per unit mass} = 4.343 \cdot \frac{\sigma_{ext}}{m} \quad (1.13)$$

The 4.343 is equal to $10 \log_{10}(e)$ the conversion factor to dB.

From figures Fig. 1.3 and Fig. 1.4 it appears to be clear the discrepancy of extinction between frequencies, at G-Band it doubles or triples the maximum extinction of W-Band, risking to occur in total attenuation in certain cases therefore it's imperative to choose an application region that suffer the least from this effect, high latitudes and polar regions seems the perfect fit as they are cold and dry, so a polar orbit would be ideal.

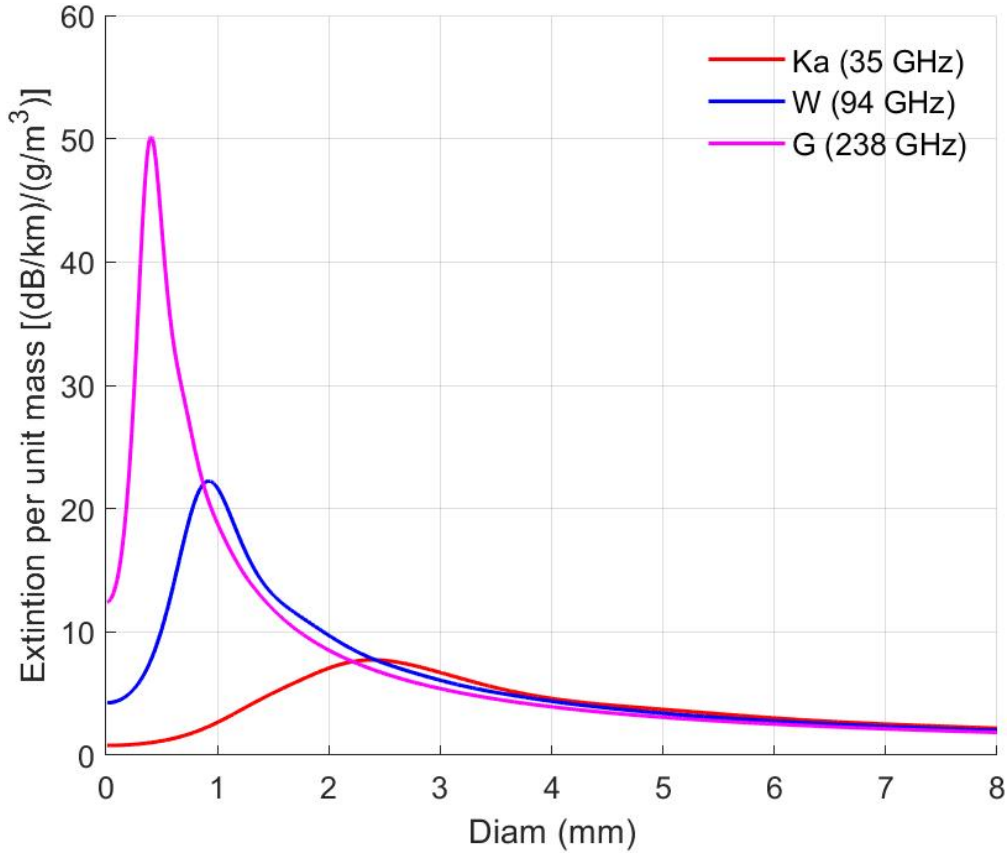


Figure 1.3: Rain extinction per unit mass at different frequencies: Ka (red), W (blue) and G (magenta); Peak extinction occurs at decreasing diameters with increasing frequency.

1.4 Particle size distribution properties

The behaviour of a single particle is useful to know theoretically what is the expected outcome of a single hydrometeor species when illuminated by the radar, but for a real life scenario particles should be considered in their totality with the presence of multiple phases at once since no cloud or rainfall contains only equal particles, therefore introducing a large variability in properties. This oscillatory behaviour is smoothed out when the integration over the particle size distribution, or population, is performed.

The concentration of particle size is generally parameterized with a Gamma function of the form

$$N(D) = N_0 D^\mu e^{-\Lambda D} \quad (1.14)$$

where D is the Diameter of the particles, the parameter μ is a unitless shape

1.4. PARTICLE SIZE DISTRIBUTION PROPERTIES

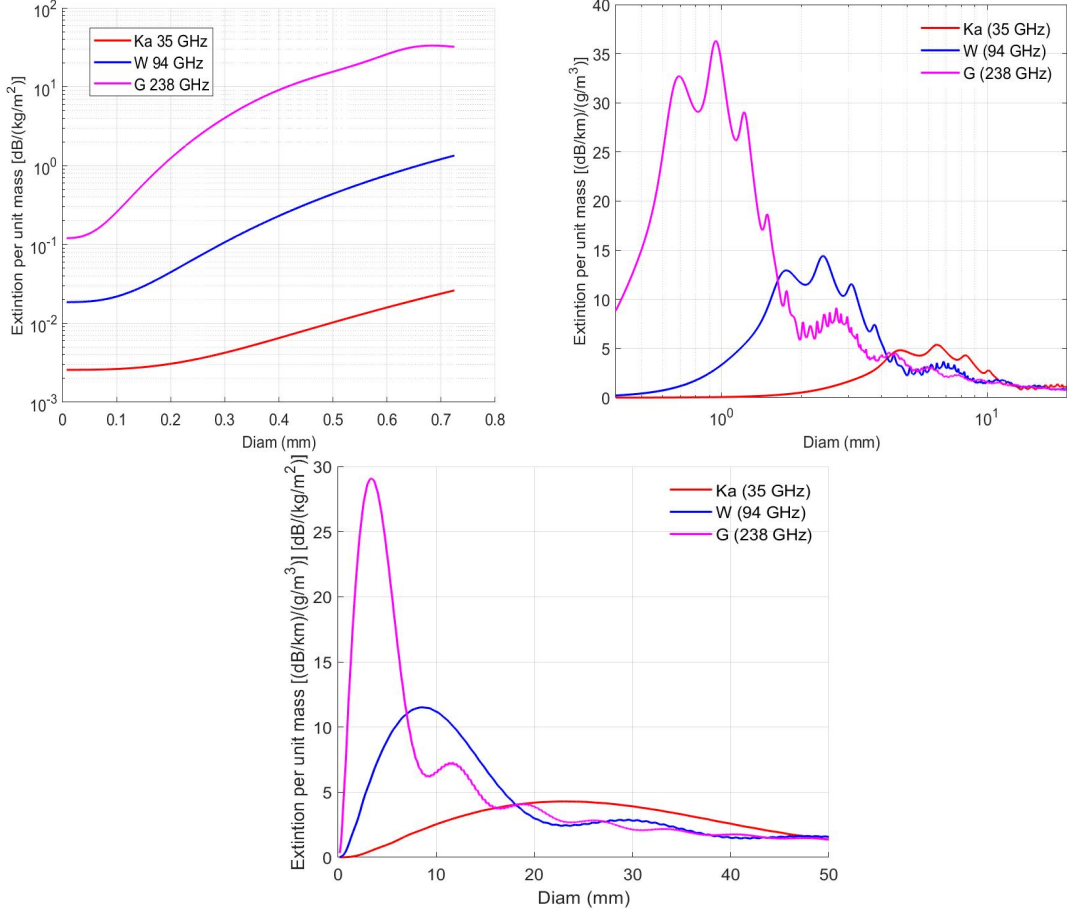


Figure 1.4: Ice (top left), Hail (top right) and Graupel (bottom) $\frac{\sigma_{ext}}{m}$ -D at different frequencies: Ka (red), W (blue) and G (magenta); Oscillating behaviour can be distinguished from rain smoother behaviour.

parameter (hereafter assumed to range between 0 and 6) and N_0 is related to the particle concentration.

Water Content is the integral of particle mass on the diameter, in millimeters:

$$WC = \int_0^{\infty} m(D)N(D)dD \quad (1.15)$$

The mean mass weighted diameter is:

$$D_m = \frac{\int_0^{\infty} D \cdot m(D)N(D)dD}{WC} \quad (1.16)$$

In case of spherical particles ($m = \frac{\pi}{6}\rho D^3$ where ρ is the particle density),

$$WC = N_0 \frac{\Gamma(4 + \mu)}{\Lambda^{4+\mu}} \quad (1.17)$$

$$D_m = \frac{\Gamma(5 + \mu)}{N_0 \Lambda^{5+\mu}} \cdot \frac{N_0 \Lambda^{4+\mu}}{\Gamma(4 + \mu)} \quad (1.18)$$

Using the property of the gamma distribution $\Gamma(n + 1) = n!$ it's possible to determine the parameter Λ in function of mean mass weighted diameter:

$$\Lambda = \frac{4 + \mu}{D_m} \quad (1.19)$$

Now keeping the equation Eq. 1.16 with WC implicit and substituting Λ with equation Eq. 1.19 is possible to determine D_m in function of WC, N_0 and μ

$$D_m = \sqrt[4+\mu]{\frac{WC \cdot (4 + \mu)^{5+\mu}}{\frac{\pi}{6} \rho_w N_0 \cdot \Gamma(5 + \mu)}} \quad (1.20)$$

Two important quantities of particle distributions are the coefficients of back-scattering and extinction (K_b and K_{ext}), divided by the mass as previously done:

$$\frac{K_b}{m} = \frac{\int_0^\infty N(D) \sigma_b dD}{WC} \left[\frac{m^2}{kg} \right] \quad \frac{K_{ext}}{m} = 4.343 \cdot \frac{\int_0^\infty N(D) \sigma_{ext} dD}{WC} \left[\frac{dB}{\frac{kg}{m^2}} \right] \quad (1.21)$$

by doing so the equation does not depend on N_0 (Normalized number of concentration [m^{-4}]) anymore.

1.4.1 Attenuation

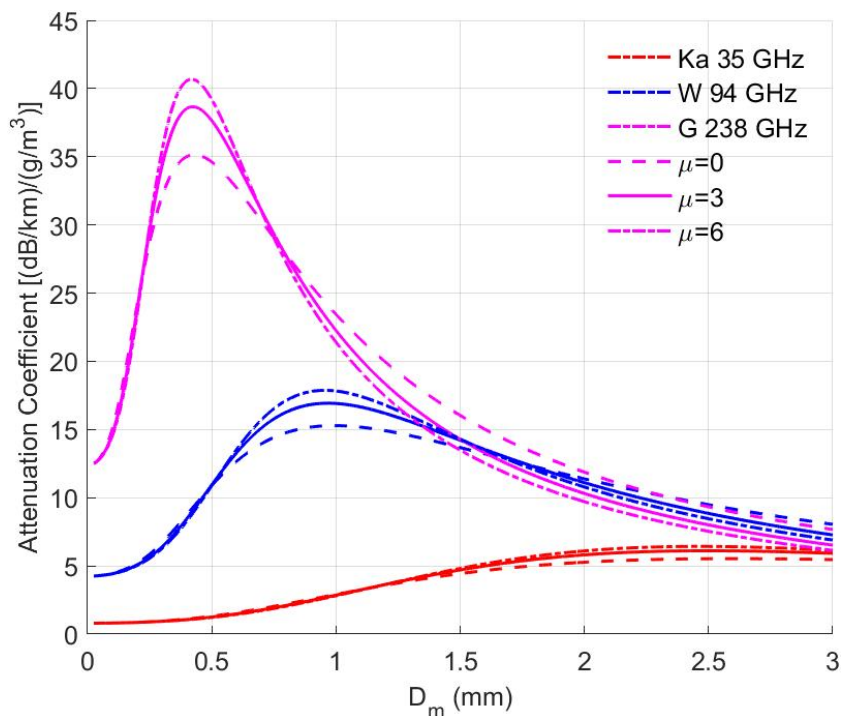


Figure 1.5: Rain extinction coefficient per unit mass at different frequencies: Ka (red), W (blue) and G (magenta) and different μ depicted with different lines; Peak attenuation occurs at decreasing diameters with increasing frequency.

It is even more apparent now that rain and cloud particles between 0.2 and 1 mm cause the maximum attenuation, of 40 dB/km every g/m^3 , because of its contribute in relation to its mass and its high probability of existing in a cloud compared to higher or lower diameter. To be able to compute the total attenuation experienced by a radar illuminating a scene it must be taken in account the contribute of every particle or aggregate of particles of different dimension and integrating in the followed path, in the case of a nadir pointed radar is exactly a 2-way path following the altitude.

From figure Fig. 1.6 it's possible to notice that for ice and snow there's a plateau in the attenuation coefficient for which single frequency retrieval cannot distinguish properly the size of the particle, therefore the water content in these phases.

1.4. PARTICLE SIZE DISTRIBUTION PROPERTIES

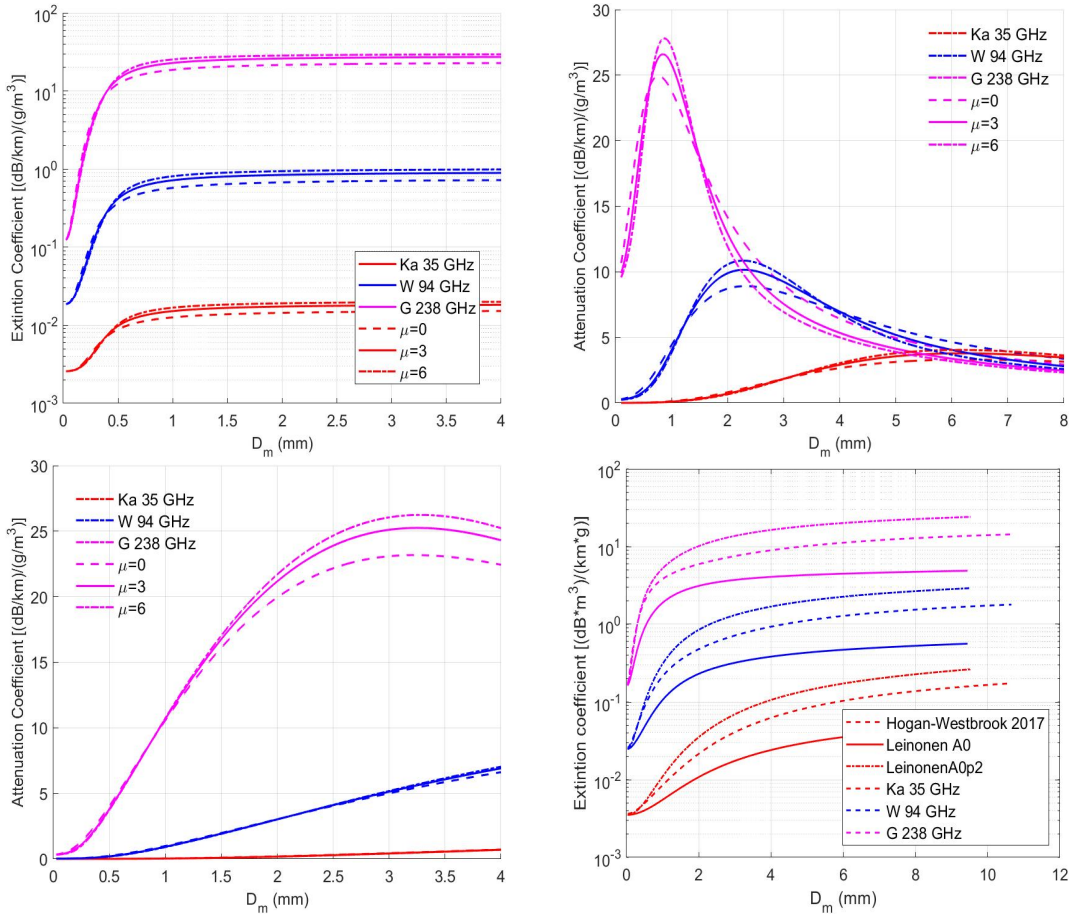


Figure 1.6: Ice (top l), Hail (top r), Graupel (bottom l) and Snow (bottom r) $\frac{K_{ext}}{m} - D_m$ at different frequencies: Ka (red), W (blue) and G (magenta) and different μ depicted with different lines; Plateaus can be spotted in ice and snow attenuation.

The attenuation experienced by a radar in function of what particle it encounter is useful to know in which scenarios works best the solution and when it could be attenuated over the limit of sensitivity, but to extrapolate information about the size and water content it is important to have differential attenuation plots:

$$\text{Diff. Att.} = K_{ext}(f_{low}) - K_{ext}(f_{high}) \quad (1.22)$$

1.4. PARTICLE SIZE DISTRIBUTION PROPERTIES

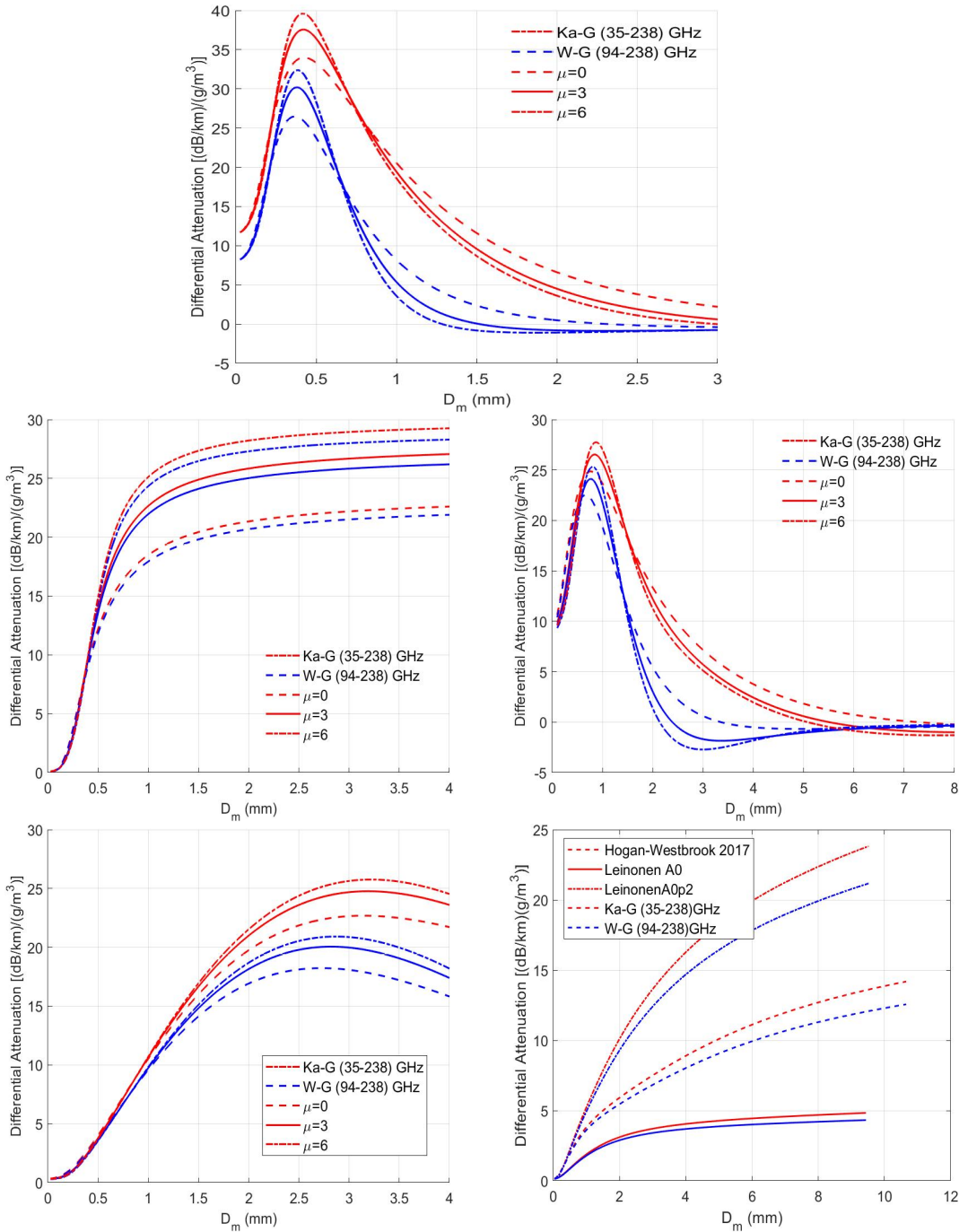


Figure 1.7: Differential attenuation Ka-G (red), W-G (blue): Rain (top c), Ice (top l), Hail (top r), Graupel (bottom l) and Snow (bottom r) at different μ depicted with different lines

Snow models

In the study are included three models of riming and snow aggregates: The first two were proposed by Leinonen and Szyrmer [2015], LeinonenA0kgm2, a model with no riming representation; LeinonenAp2kgm2, a model with heavy riming, lastly Hogan and Westbrook 2017 for an all purpose model. Scattering properties have been computed with the self-similar Rayleigh-Gans approximation [Hogan and Christopher D. Westbrook 2014;Hogan, Honeyager, et al. n.d.;Leinonen et al. n.d.].

Riming is a process of converting liquid cloud water into ice and plays an important role in the formation of precipitation in cold clouds, snowflakes collects supercooled liquid water droplets, which freeze and merge on contact. It's important also for wet removal of aerosols from the atmosphere [Baltensperger et al. 1998] and has an impact on the spatial distribution, extent and lifetimes of clouds and on precipitation efficiencies, [Lee 2011].

It's important to note that from figures Fig. 1.7 and Fig. 1.8 the model doesn't change much the differential reflectivity received, but does significantly change the differential attenuation nearly doubling from model to model.

1.4.2 Reflectivity

The information of attenuation is useful to gauge the water vapour content but it's not a direct product since it's not possible to know the right amount of signal attenuated not knowing the water content, in contrast reflectivity (Z) is a direct radar product that measure how much signal is scattered towards the radar (back-scattered). It is a function of wavelength (λ) and dielectric factor (K), as done previously is divided by the mass to eliminate the dependence to N_0 :

$$\frac{Z}{m} = \frac{K_b \lambda^4}{\pi^5 K^2 \cdot WC} \left[\frac{mm^6 \setminus m^3}{g \setminus m^3} \right] \quad (1.23)$$

From equation Eq. 1.4 is useful to express it in dBZ as the reflectivity has a vast range of possible values depending on the variables above, while in dBZ it ranges from -80 to 50. What it is of interest of this work though is the differential reflectivity or Dual Frequency Ratio (DFR) of a dual-frequency radar system:

$$DFR = Z(f_{low}) - Z(f_{high}) \quad (1.24)$$

There is another confirmation that for small mean diameters in all hydrometeors there's the possibility of discerning a differential signal that is always stronger in the Ka-G pair, meaning that this system could be more accurate with a low sensitivity. Note that raindrops produce a non-zero DFR in the Rayleigh region because we are using the convention of $\text{mod } K^2 = 0.93$.

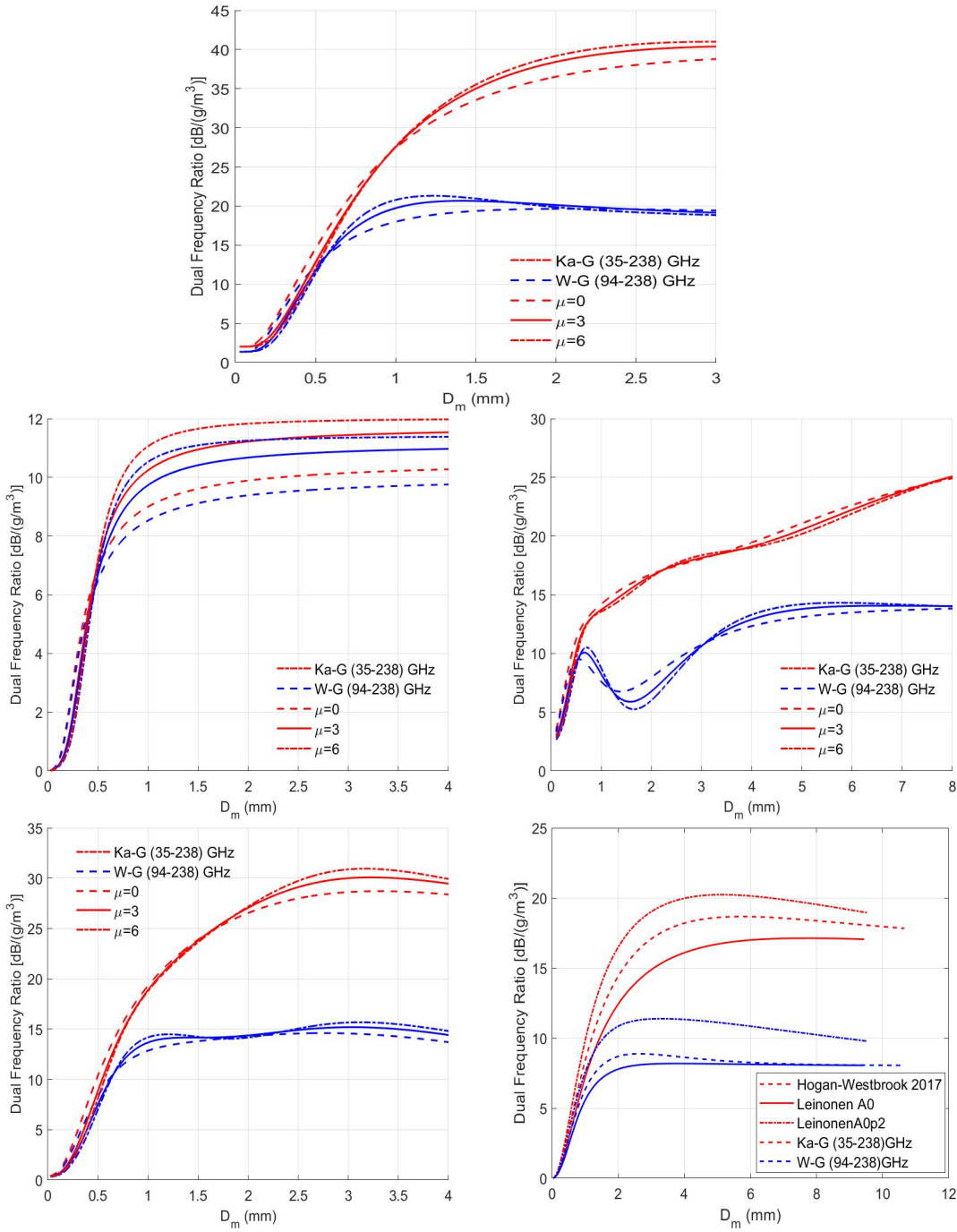


Figure 1.8: Dual frequency ratio per unit mass Ka-G (red), W-G (blue): Rain (top c), Ice (top l), Hail (top r), Graupel (bottom l) and Snow (bottom r) at different μ depicted with different lines

Chapter 2

Simulator of a space borne Ka-W-G Band radar system

This chapter describes a space-borne radar simulator for cloud radars with frequency spanning from Ka to the G-band. The simulator is fed with data from CloudSat mission and ECMWF from 2007 and 2008; This dataset allows to determine the global statistics of radar observations at the resolution of actual space borne radar placed in the same polar sun-synchronous orbit as CloudSat. A validation of input data was necessary to be sure of it being aligned with ground based measurements Then making use of the knowledge exposed in chapter one, single particle scattering properties tables are used to characterize the hydrometeor population in its entirety and to proceed to generate radar observables as reflectivity and PIA from CAPTIVATE. At the end examples of case studies divided in low medium and high latitude events will be discussed to bring better understanding of frequency bands peculiarities and best use scenarios.

2.1 Simulator input: the CAPTIVATE database

CAPTIVATE is an algorithm that exploited data from CloudSat (that operate at 94GHz) with its CPR (Cloud Profiling Radar, [Tanelli, Durden, et al. 2008]) in combination with the CALIOP lidar of CALIPSO and the MODIS radiometer in the A-Train constellation in low polar orbit with a vertical resolution of 60 m and an along-track horizontal resolution of 1.5 km [Mason et al. 2022], its characteristics allows to determine the global statistics of radar observations at the resolution of actual space borne radar, rather than being constrained by a model resolution. It retrieved three classes of hydrometeors: ice, cloud and rain with mass contents for all and characteristic sizes (D_m and N_0) for ice and rain only. Reflectivity and hydrometeors properties was obtained from CloudSat while ECMWF auxiliary

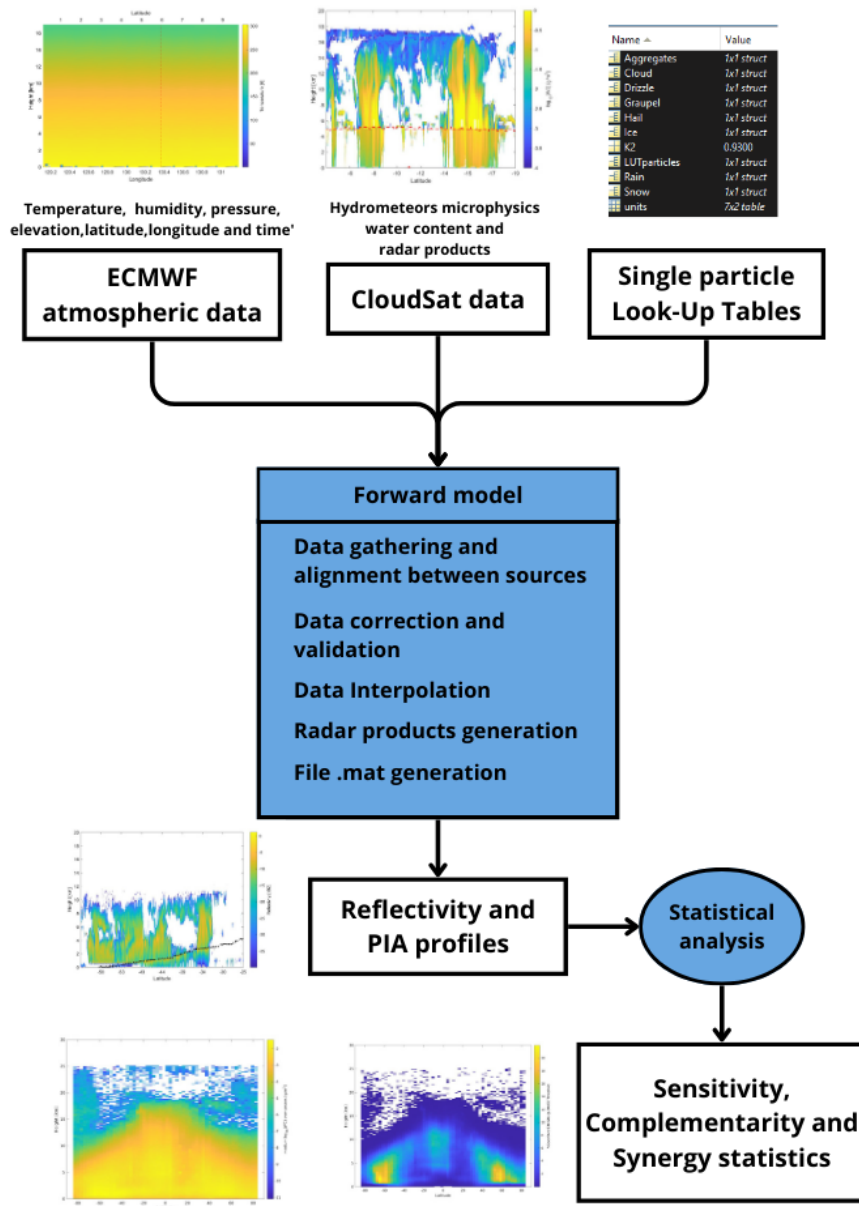


Figure 2.1: Simulator flow chart

data are used as input for temperature, pressure and relative humidity, allowing the calculation of gas attenuation.

2.1.1 Dataset used for scene generation

These data sources has been chosen over existing models because they produced plentiful of reliable data over the last decades in an orbit that fit the objectives of this technology simulator, surveying most of earth surface over the year especially over high latitudes as shown in figure Fig. 2.2, even if the time spent over latitudes is the same, the coverage of high latitudes is more thanks to the high inclination polar orbit. In particular CloudSat was placed in a sun-synchronous orbit with an altitude of 685 km, an inclination of 98.2° , and a period of 98.3 minutes.

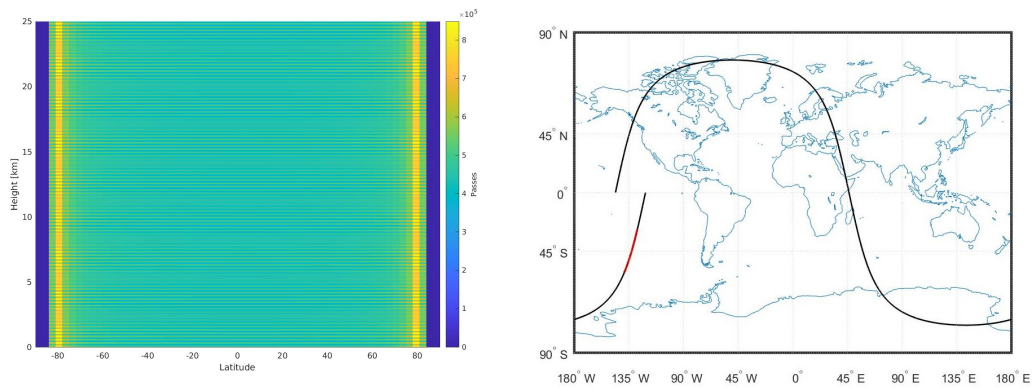


Figure 2.2: CloudSat passes over latitude (left) and sample Orbit on Feb. 15 2008 (right)

The simulator is built in MatLab and utilize more than 1500 orbits in the range of two years, covering a major part of the annual weather variability, as it can be seen in figure Fig. 2.3. In the dates from 31th march to 30th April, from 30th May to 29h July and from 19th September to the last day of the year there's no data coverage, so it is mostly winter data with some spring and summer coverage with no fall data. This concentration of data in winter time led to an excessive presence of humid season in the southern hemisphere overestimating LWP and underestimating surface detection at these latitudes.

From chapter two's theory base a database of single particle characteristics was constructed, called Look-Up Tables (LUT), and used in this simulator with a 3-dimensional interpolator to fill the gaps of particle dimension, μ parameter and Temperature in the grid thus extrapolating from the gridded values of the tables any value of single particle characteristics within the range, e.g. back-scattering cross section.

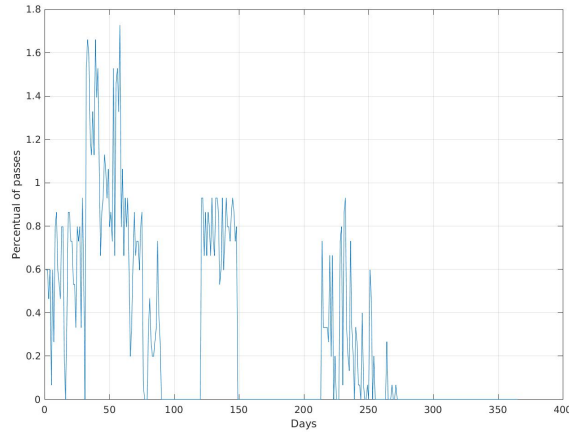


Figure 2.3: Annual data distribution in linear days from first January showing a lack of data in summer and fall

The retrievals of CAPTIVATE and ECMWF data, for example, of water content comes in form of a matrix as shown below in figure Fig. 2.4.

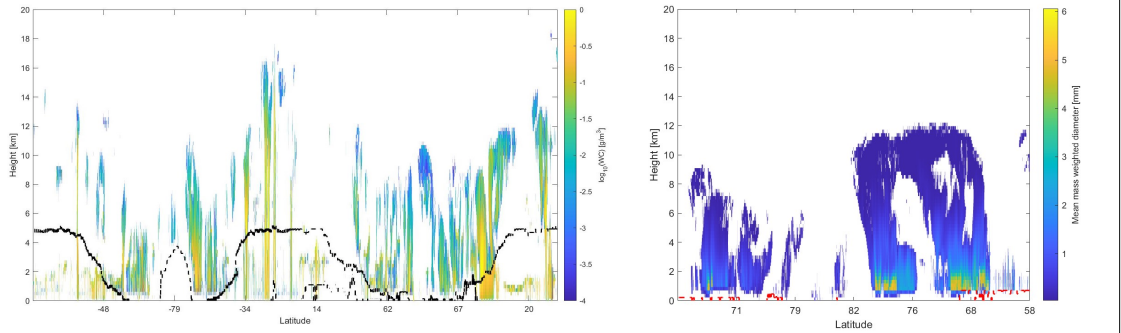


Figure 2.4: Water content of all hydrometeors profile of a full orbit (left), characteristic diameter of rain (right) black and red line represent 0°C iso-thermal

It can be noticed different atmospheric systems within the orbit with different depths and precipitation but it's useful to separate high, mid and low latitude events to better notice advantages and disadvantages of the three frequencies.

2.1.2 CAPTIVATE statistics of microphysical properties

The data obtained have already been checked by ECMWF but to eliminate some background noise and smooth out the results has been operated a correction where

hydrometeors content above the 99th percentile calculated on positive values are replaced by an average over adjacent observations. To be sure that the characteristic diameter and particles number distribution of the dataset is aligned with current research and knowledge in figure Fig. 2.6 there is a replica of Dolan paper [Dolan et al. 2018] results in figure Fig. 2.5. The original figure have low characteristic

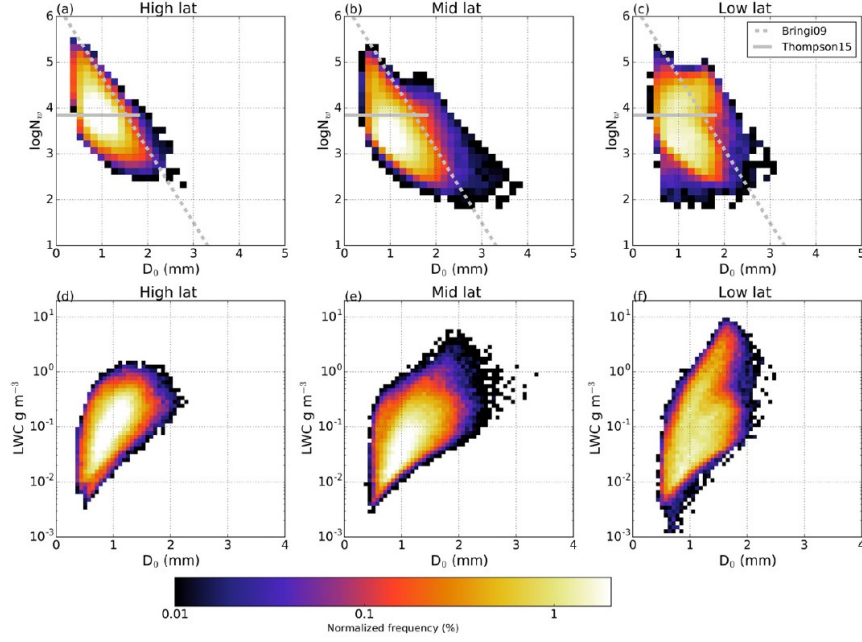


Figure 2.5: Two-dimensional normalized frequency of occurrence as a function of latitude band for (a)–(c) $\log(N_w) \sim D_0$ and (d)–(f) LWC– D_0 of (Dolan et al. 2018) paper .

size limitations due disdrometer limitations, on the other hand the replica plot has upper LWC limitations due to CAPTIVATE retrieval limitations.

The differences in $\log_{10}(N_w)$ are due to a difference in units of measurement, in figure Fig. 2.5 are in $[mm^{-1}m^{-3}]$ and in figure Fig. 2.6 are in $[m^{-4}]$, but apart from that the trend is the same.

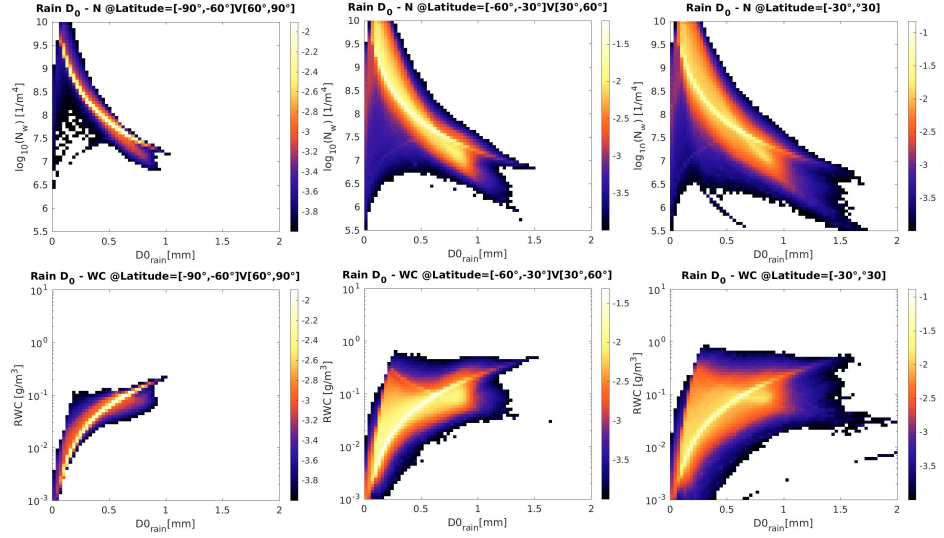


Figure 2.6: Two-dimensional normalized frequency of occurrence as a function of latitude band for (a)–(c) $\log(N_w) \sim D_0$ and (d)–(f) LWC– D_0 replica.

2.2 Simulation of radar observables

The sensitivity threshold for the three frequency system are chosen on the base of existing technology or current studies funded by ESA [G band project team 2024]; radar characteristics are presented in Fig. 2.7 divided results as shown in table 2.1

Satellite	Frequency [GHz]	Nominal sensitivity [dBZ]
CloudSat	94	-30
GPM (Ka band)	35.6	12/15
EarthCare	94	-36
SCOUT	238	-14.5
Earth Explorer	35	-30
Earth Explorer	238	-33.5
This study band:		
Ka	35	10/-20
W	94	-10/-30
G	238	-10/-40

Table 2.1: Past and future missions frequency divided sensitivity comparison with this study sensitivities choice

Radar Mode				
Pulse scheme	Pulse		Chirp	
	Frequency diversity 3.3 μ s unmodulated (ref)		Max pulse 99 μ s NLFM pulse with B = 0.3 MHz	
Range resolution (m)	500		500	
MDS no integration (dBZ)	+10.0		-1.7	
Integration length (km)	1			
Number of samples (#)	357			
Independent samples	357			
MDS with integration (dBZ)	-2.7		-14.5	
Random error after Integration assuming 20 dBZ target return level (dB)	0.252		0.231	

Radar Mode				
Pulse scheme	Pulse		Chirp	
	Frequency diversity 1.66 μ s unmodulated (ref)	Max pulse 20 μ s NLFM pulse with B = 0.6 MHz	Frequency diversity 1.66 μ s unmodulated (ref)	Max pulse 20 μ s NLFM pulse with B = 0.6 MHz
Range resolution (m)	250	250	250	250
MDS no integration (dBZ)	-14.7	-22.5	-19.8	-17.6
Integration length (km)	0.5		0.5	
Number of samples (#)	158		158	
Independent samples	158		158	
MDS with integration (dBZ)	-25.7	-33.5	-20.8	-28.6
Random error after Integration assuming 20 dBZ target return level (dB)	0.346	0.346	0.346	0.346

Figure 2.7: SCOUT G-band radar characteristics (top panel) and Earth Explorer (bottom panel) G-band (second and third columns) and Ka band (fourth and fifth columns) radar characteristics.

The simulator gather and align the different datasets one orbit at a time, it operate a validation and correction upon it to avoid non realistic values due to imperfections and noise in signal retrieval. After that with the use of single particles properties listed in a Look-Up table, constructed as discussed in the previous chapter, interpolates data and provide through the algorithm modeled radar products as reflectivity and PIA. The products are then combined to produce surface attenuated reflectivity then to be added with hydrometeors attenuated reflectivity to get total attenuated reflectivity.

2.3 Example of cases studies

Here case studies from single orbits are presented to highlight pros and cons of single and dual frequencies radar system; precipitation events with high convection and altitude development are divided in high, medium and low latitude:

2.3.1 High latitude

High latitude scenes as shown in figure Fig.2.8 are characterized by icy clouds and frozen precipitation, like snow, because of the strict temperatures that don't

exceed 0°C at surface level. It can be noticed that neither Ka, W or G experience high attenuation proceeding towards the ground, that's because, as seen in figure Fig. 1.6, small particle of ice generate at most 10dB of attenuation per gram over cubic meter for G-band and risible values for Ka and W. Even though this could be a snow precipitation event with larger diameter snowflakes G band produce reflectivity well within the selected sensitivity intervals of -20/-40dBZ while to be able to detect such small particles sophisticated systems for Ka and W are required seen that their sensitivity stands on the lower selected sensitivity. From figure below and figure Fig. 2.4 water content is detected as low as $0.01 \frac{g}{m^3}$ and particles as small as fractions of millimeter by G-band while W and Ka ($0.1 - 0.5 \frac{g}{m^3}$) of WC and (1;2)mm of particle size.

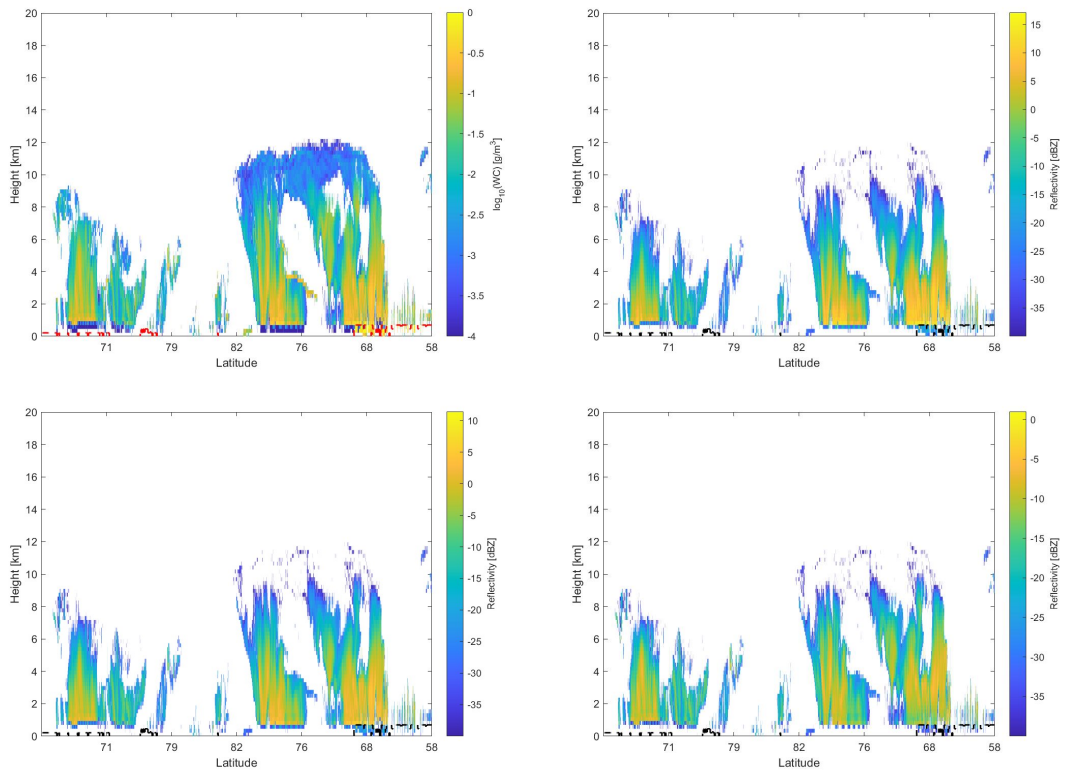


Figure 2.8: High latitude case study: Water content (top l) Reflectivity in Ka (top r), W (bottom l) and G (bottom r) profiles of an event of icy precipitation on February 15th 2008 over Arctic circle and Svalbard islands. Pay attention that plot color scales differs from one another

2.3.2 Mid latitude

Mid latitude systems are characterized by mixed layers of cloud and precipitation, typically high icy clouds with cloud top up to 13 km with rain that could start high up at 3-4 km, depending on the season, derived from melting snow (cold rain process) or condensed cloud (warm rain process). Fig.2.9 shows perfectly the case

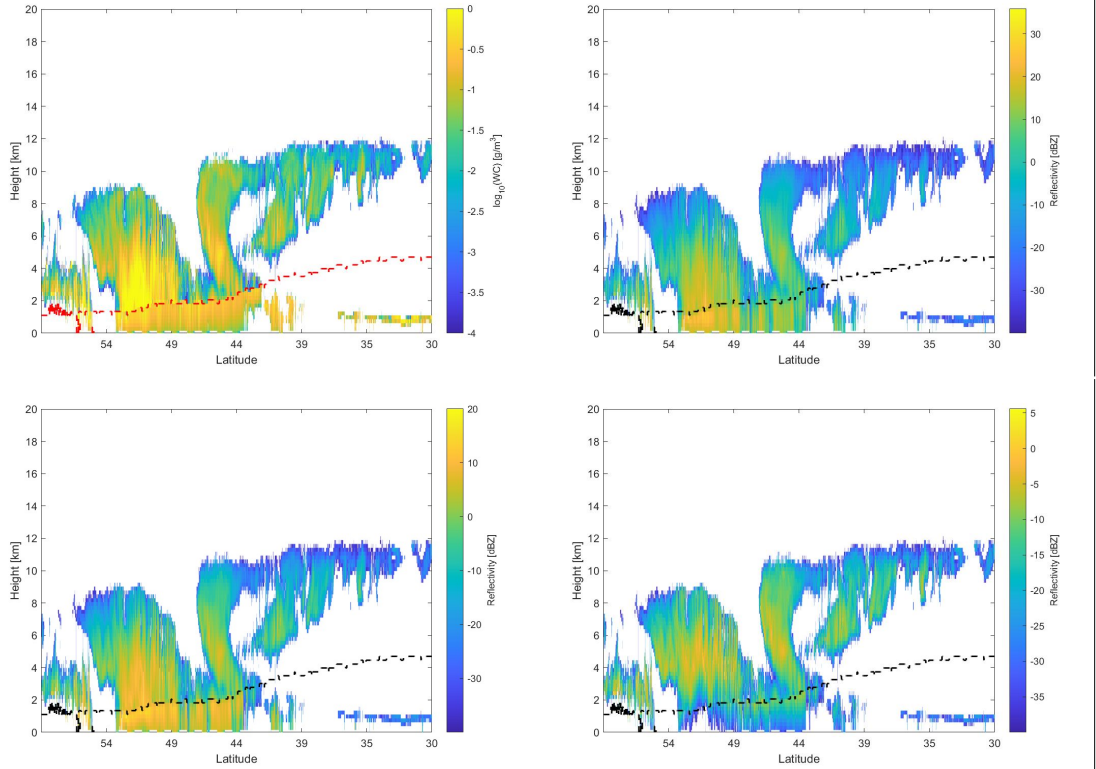


Figure 2.9: Mid latitude case study: Water content (top l) Reflectivity in Ka (top r), W (bottom l) and G (bottom r) of a mixed phase cloud system with liquid precipitation on 2nd January 2007 over Atlantic ocean west of Washington state. Pay attention that plot color scales differs from one another.

where is possible to distinguish two regions, one is above the red line where there is an icy cloud mixed with snow where is more dense and one below the red line which represents the rainfall and low cloud region on the right, the red line depicts the iso-thermal 0°C. In this case attenuation starts to play a role in G band reflectivity as rain and snow particles attenuate completely the signal under the threshold of -40dB the region with the most intense rainfall whilst Ka and W strive in this situation with tens of dBZ of return. In contrast is confirmed the ability to detect cloud top and shallow boundary layer clouds by G band in the rightmost part of

figure Fig. 2.9 making a perfect case for complementary studies.

2.3.3 Low latitude

Tropical events are characterized by heavy rainfall events that can have origin up to 4-5km in altitude [Anders and Nesbitt 2015]; clouds are characterized by a greater mean size than those in high and mid latitude regions due to their high water content as shown in the first panel on the top left of figure Fig. 2.10. Because of this difference clouds are well detected by Ka and W band but the attenuation, also caused by high water content, hits the two as well as G band that result completely attenuated at the turn of the melting point preventing the detection of anything below that altitude. A suitable system for the detection would comprehend a Ku-band radar, a typical precipitation radar, but it's not in the interest of this study. The domain of application of G-band radar remain cloud top detection with the possibility of a synergistic approach.

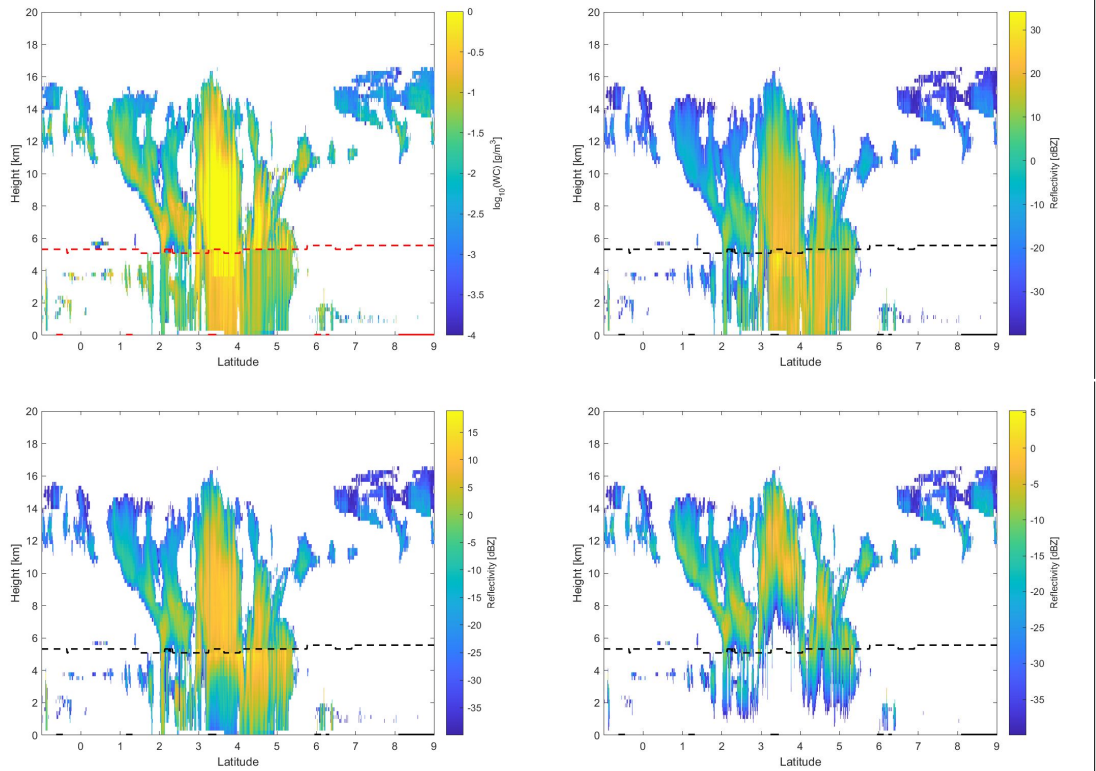


Figure 2.10: Low latitude case study: Water content (top l) Reflectivity in Ka (top r), W (bottom l) and G (bottom r) on January 3rd 2007 over central Africa. Pay attention that plot color scales differs from one another.

Imperfections in the signal could be noticed, it is caused by faulty CAPTIVATE retrieval.

2.3.4 Preliminary discussion on the potential of a dual frequency system including a G-band radar

In the regions where all of the radar signals remain above their minimum detectable signal (MDS) they can be exploited synergically for retrieving cloud micro-physical properties, thus reducing the uncertainties associated with single-frequency retrievals. In contrast where there's no DFR it could be because one of the radar signal see and the other don't, and it comes into play the complementarity, the two signals complete each other by providing data where the other isn't capable of detecting a signal.

It can be seen from figure Fig. 2.11 that Ka-G pair produce stronger differential signal than W-G pair in any case although it is not true that greater DFR are better, because at those extreme values of over 40 dB we must remind that one of the systems is working on its threshold limit of detection, thus providing little information about differential signal but getting closer to the stronger signal of the pair. The optimal interval of a differential signal is [3;20]dB, and synergy between the two could be pursued gathering additional information from differential absorption and non Rayleigh effects. In the high latitude event all the profile is in this optimal region making an ideal candidate for synergy studies. The mid latitude event show a limited synergy possibility in case of heavy/moderate rain but for the part above the melting point synergy is possible, making it a candidate for both synergy and complementary studies. In the low latitude event synergy is at most impossible seen that G band could not penetrate under five kilometers, but is the right case for complementary studies between low troposphere and cloud top.

2.3. EXAMPLE OF CASE STUDIES

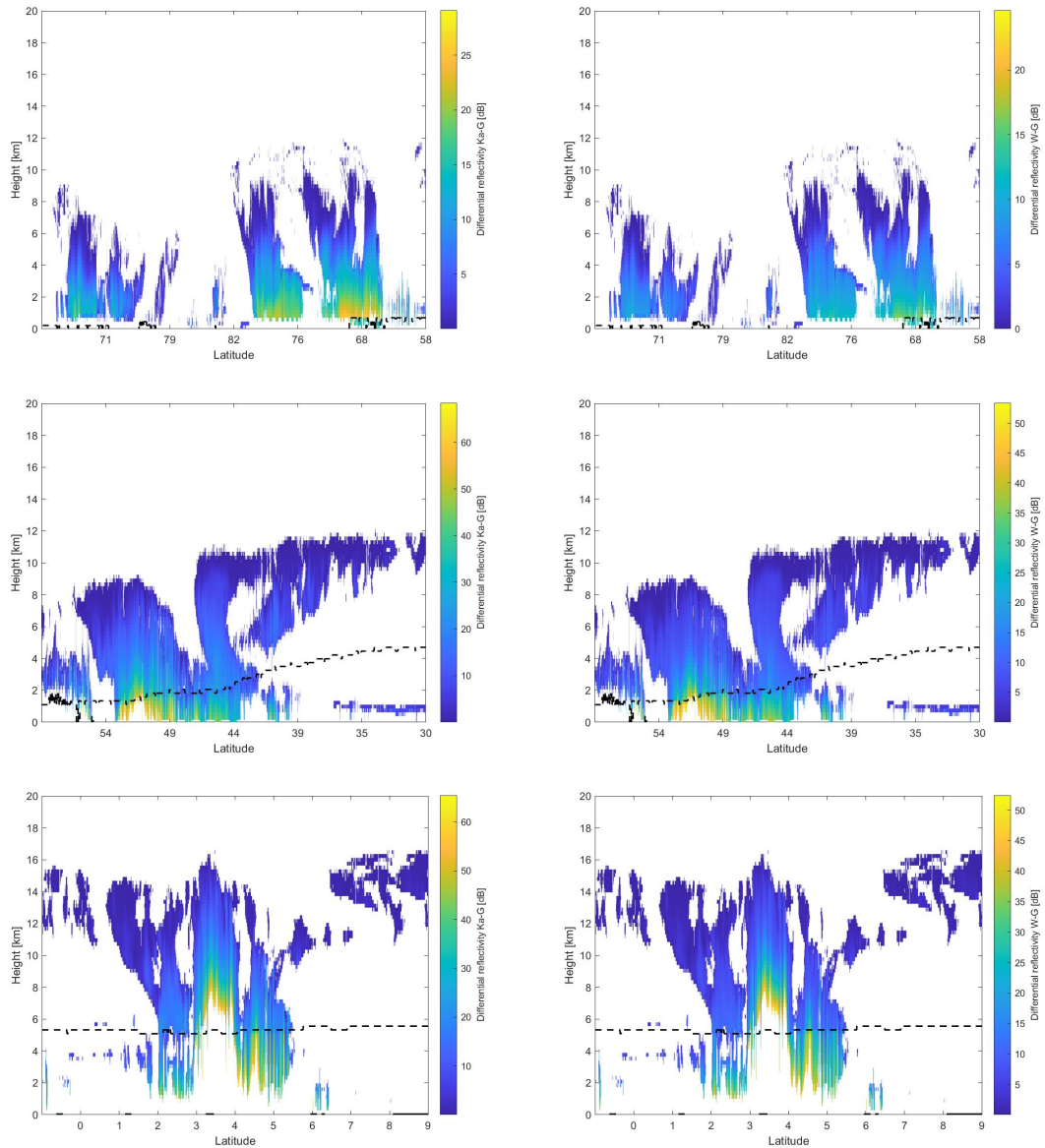


Figure 2.11: DFR of previous case studies: Ka-G (left column) W-G (right column), high latitude (top row), mid latitude (mid row) low latitude (bottom row). Pay attention that plot color scales differs from one another

Chapter 3

Statistical analysis of single frequency sensitivity and of complementarity and synergy for the Ka-G and W-G frequency pairs

The aim of this analysis is to characterize how well a low-high frequency pair (Ka-G and W-G) would detect clouds at different latitudes and heights when considering a full year climatology. The focus of this analysis will be at assessing synergy and complementarity for the two frequency pairs Ka-G and W-G. Ultimately this analysis will prove that a G-band system will enable to better characterize ice clouds at high altitudes in low latitude regions and in the whole troposphere at high latitudes. This improvement is underpinned by the higher sensitivity of G-band systems and by the potential of exploiting the high DFR and differential PIA that Ka-G pair produce to retrieve smaller characteristic diameters and smaller liquid water path.

Normally different frequency bands are used to detect certain targets. The so called cloud radars are suitable to detect light to medium precipitation that produce low/intermediate attenuation levels not strong enough to drive the signal below the detection level; on the other hand such radars experience significant attenuation in heavy rain conditions. In contrast Ku band systems like the TRMM and GPM PR are well suited for moderate/heavy rain conditions but have poor performance in light precipitation because of their reduced sensitivity (see 2.1).

From cloud radars radiative forcing can be inferred, thus cooling and heating rates; from precipitation radars latent heat could be derived. Since Ka is between being a cloud and a precipitation radar it is useful to pair it up with G-band that is a cloud radar able to detect small particles of clouds up to the upper troposphere. Synergistic retrievals has the advantage of overcoming the limitation that single-instrument retrievals can be subject to, e.g. uncertainties in complex or multi-layered scenes.

3.1 Statistical analysis characteristics

As a statistical study radar products needed to be sampled in gridded bins, some better suited a linear grid like D_0 , Latitude, Altitude and DFR while some a logarithmic grid seen the broad values range.

	# of points	Range
Latitude	91	$[-90^\circ; 90^\circ]$
Altitude	242	$[0; 25]$ km
$\log_{10}(RWC)$	65	$[10^{-3}; 5] \frac{g}{m^3}$
$\log_{10}(IWC)$	65	$[10^{-4}; 20]$
$\log_{10}(CWC)$	65	$[10^{-5}; 10]$
<i>ice</i> D_0	70	$[0; 4]$ mm
<i>rain</i> D_0	70	$[0; 2]$ mm
<i>rain</i> $\log_{10}(N)$	70	$[10^{5.5}; 10^{10}] m^{-4}$
<i>ice</i> $\log_{10}(N)$	70	$[10^3; 10^{10}] m^{-4}$
DFR	103	$[0; 50]$ dB

Table 3.1: Table of radar products grid number of points and value range

3.2 Statistical sensitivity analysis of single frequency radar

The goal of this section is to understand at what altitudes and latitudes a single frequency system could detect atmospheric systems (cloud and precipitation) by characterizing the relative frequency of detection relative to the number of satellite overpasses for the specific location. The data used for this analysis and the next one is hydrometeors reflectivity filtered off of surface reflectivity to bring clearer results under 2 km.

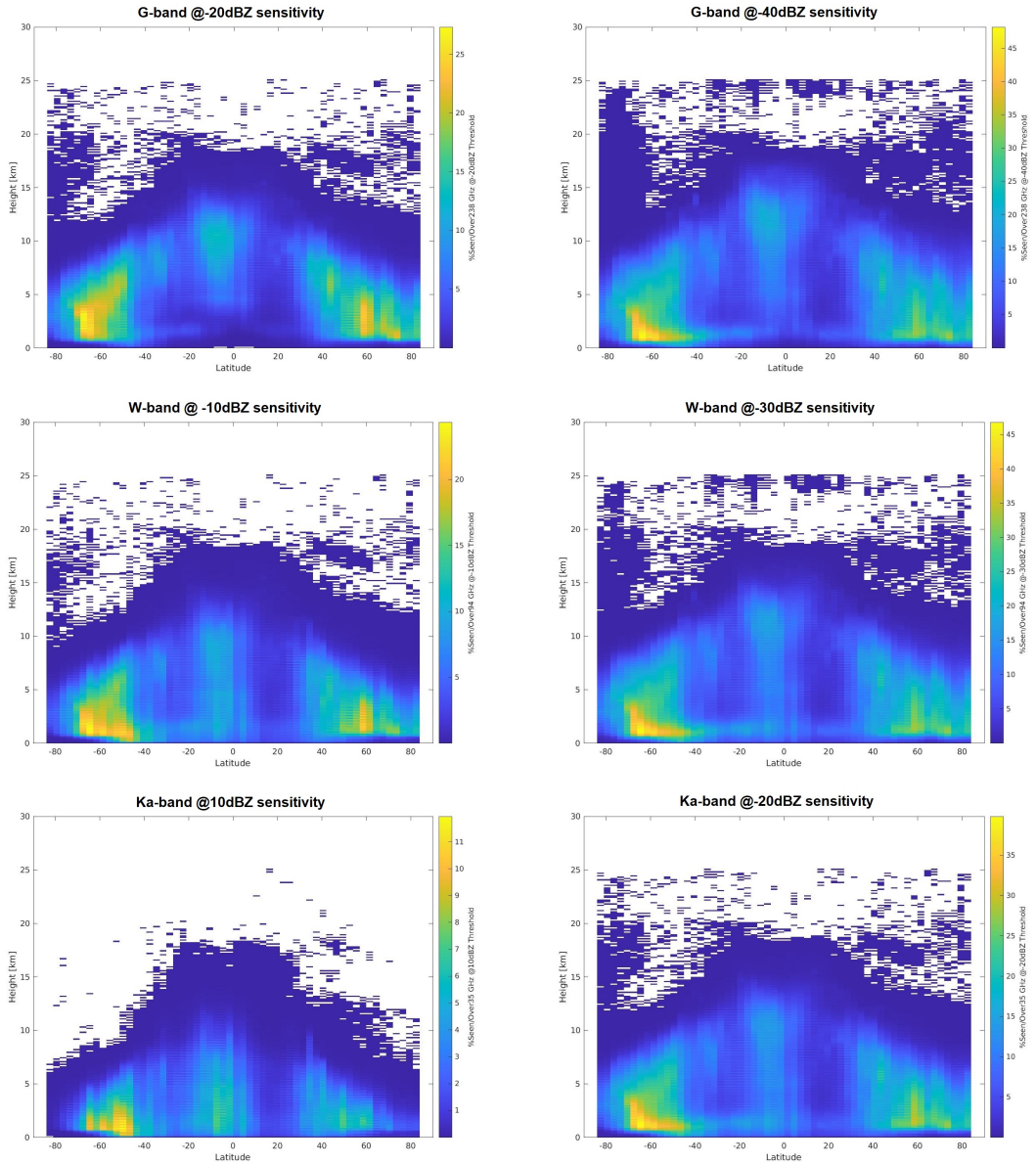


Figure 3.1: Statistical detection percentage in a zonal plot of G band radar at -20dBZ (first row, left panel) and -40dBZ (first row, right panel). W band at -10dBZ (second row, left panel) and -30dBZ (second row, right panel) and Ka band at 10dBZ (third row, left panel) and -20dBZ (third row, right panel). Pay attention that plot color scales differs from one another

The top left panel in Fig. 3.1 demonstrates that even a low sensitivity G-band radar can detect up to 15% and 25% of the time high latitude and high

altitude systems, with better performance compared to W and Ka low sensitivity counterparts that detect better low and mid altitudes events. This difference create a foundation for what to expect in complementarity analysis. High sensitivity systems (right panels) despite being difficult to assemble in a compact satellite for a LEO orbit have all similar detection capabilities with peaks of 65% and minimum of 20% of detection; but what doesn't appear in this graph is the different nature of detected target, one could be mistaken to think that G-band and W-band are similar since they share similar detection areas and values. G-band in fact detect smaller targets (e.g ice clouds top) than W band, it is merely noticeable but comparing top right panel with middle right panel values of detection are a bit higher and extends over the 15km line.

3.3 Statistical synergy and complementary analysis of frequency pairs Ka-G, W-G

In this section will be sought the complementary and synergistic relation between dual frequency systems Ka-G and W-G. In particular the aim of the synergy analysis is to investigate where are the optimal synergy regions (with a DFR signal in the range between 3 and 20 dB) and characterize it as the sensitivity of frequency bands changes. Complementary analysis seek areas with one signal of the pair that can't detect any signal and one that detect above its sensitivity threshold so that radar returns can complete each other with information on areas where otherwise there would be no information on. Particularly at low-mid latitudes where mixed phase clouds are more common and a single frequency approach could not make the picture of the entire event.

The probability distribution function of DFR for three different regions as identified in Fig. 3.4 is depicted in Figs. 3.2, 3.3. These regions were purposely selected to bring to light the differences in signal differential in key G-band and Ka/W-band application areas.

In figure (Fig.3.2) is represented the optimal synergy region in the tropics, at altitude 2km and latitude 0° , for the pair W-G. Tropics presents a high mean DFR due to the difference between attenuated G-band signal and high signal levels from both W and Ka; nevertheless the majority of the passages are in the optimal region, this suggests that this frequency pair, Ka-G, are complementary to each other. This differential interaction with the environment could be beneficial to better understand different aspects of the atmospheric systems in this region (represented as the yellow band in bottom right fig.3.4).

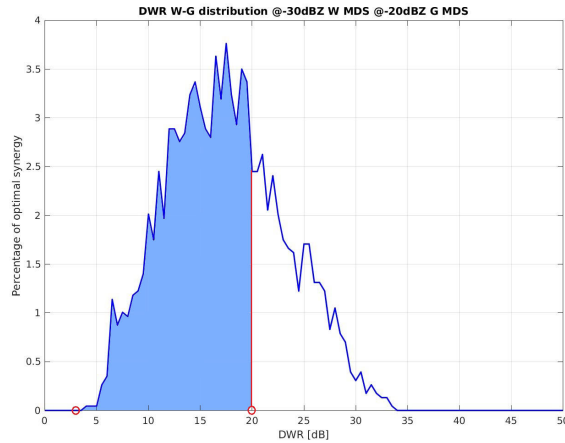


Figure 3.2: W-G DFR distribution at latitude 0° and altitude 2km, red bounds represent optimal synergy bounds and light blue region represent optimal synergy region.

Another case of DFR distribution is represented in left fig.3.3, this mid-latitude (-52°), mid-altitude (5km) shows a lower mean DFR and the distribution of DFR has the majority of its values inside the optimal region. That is because of both frequency detecting events with a good signal, never experiencing such attenuation to cancel the signal. This suggests that in this region (represented as the yellow band in top right fig.3.4) a good synergy could be exploited between frequency pairs, combining the results a better understanding of atmospheric events microphysics and water content could be obtained.

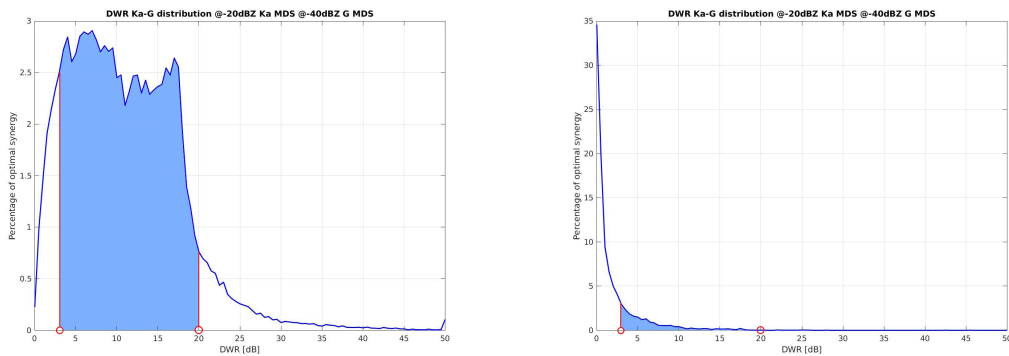


Figure 3.3: Ka-G DFR distribution at latitude -52° and altitude 9km (left) latitude -52° and altitude 9km (right), red bounds represent optimal synergy bounds and light blue region represent optimal synergy region.

The last case that is presented is a low latitude (-12°), high altitude (14km) in right figure Fig.3.3. High sensitivity G-band (-40dBZ) has the advantage of detecting particles up to millimeters (see figure Fig. 2.8), typical of cloud tops, but neither Ka or W band could detect them, even with high sensitivity systems. Positive and high DFR means that Ka-band is detecting with a stronger signal than G-band, but that's not the case at such high altitudes. When they detect simultaneously is always with such low difference that the DFR distribution results shifted towards zero. Comparing the three figures Fig. 3.2, 3.3 a pattern of shifting DFR distribution from low mean values to high mean values can be noticed going from high altitudes, through the optimal region (the bridge shaped yellow band in figure Fig. 3.4), to low altitudes at tropics.

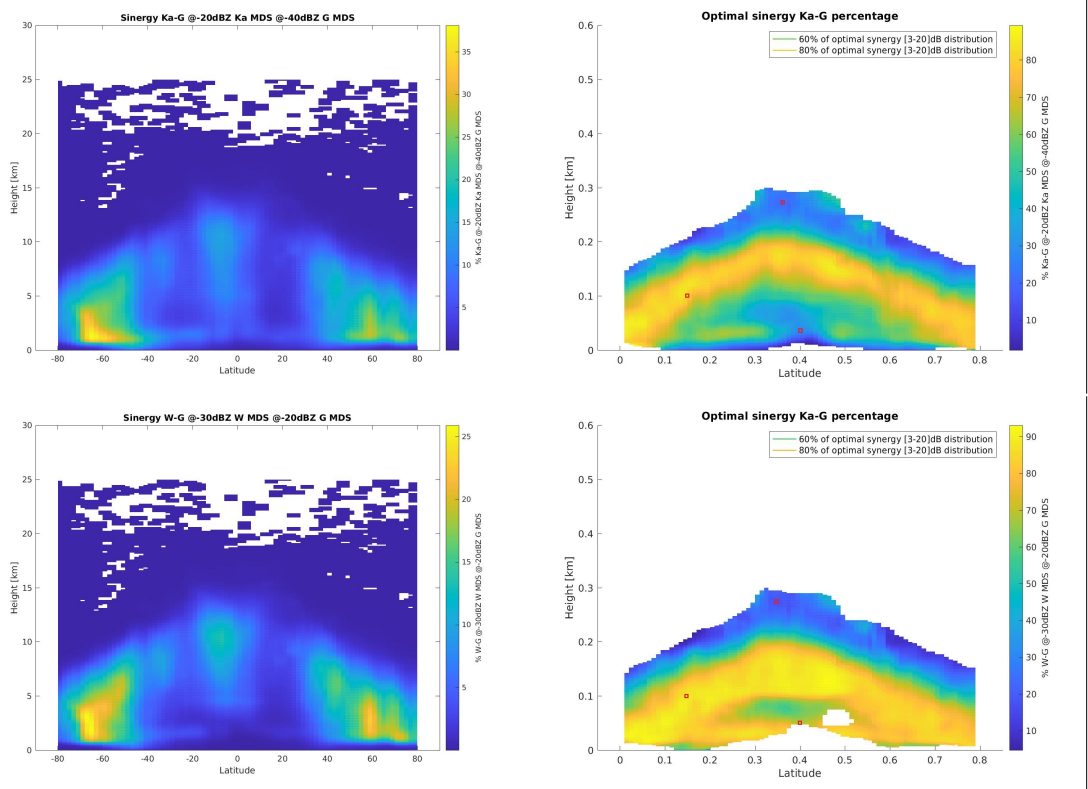


Figure 3.4: Statistical synergy detection percentage in a zonal plot of Ka-G (top left) with -20dBZ and -40dBZ sensitivity threshold and W-G (bottom left) with -30dBZ and -20dBZ sensitivity threshold. On the right the optimal synergy percentage of DFR. Red squares represent the sampled region for Figs. 3.2-3.3. The percentage is the ratio of the blue region and the total area times 100 in figure Fig. 3.2. Notice that plot color scales differ in the different panels.

3.3. STATISTICAL SYNERGY AND COMPLEMENTARY ANALYSIS OF FREQUENCY PAIRS KA-G, W-G

As it can be seen synergy works best at high altitudes in the Tropical belt and in the whole troposphere in mid-high latitude area, as expected due to the strong attenuation associated to water vapor for G-band radars. Estimates based on this statistical analysis suggest that at most 25% and 35% of the times synergy is possible between moderate sensitivity W and G band and very high sensitivity Ka and G-band systems, respectively.

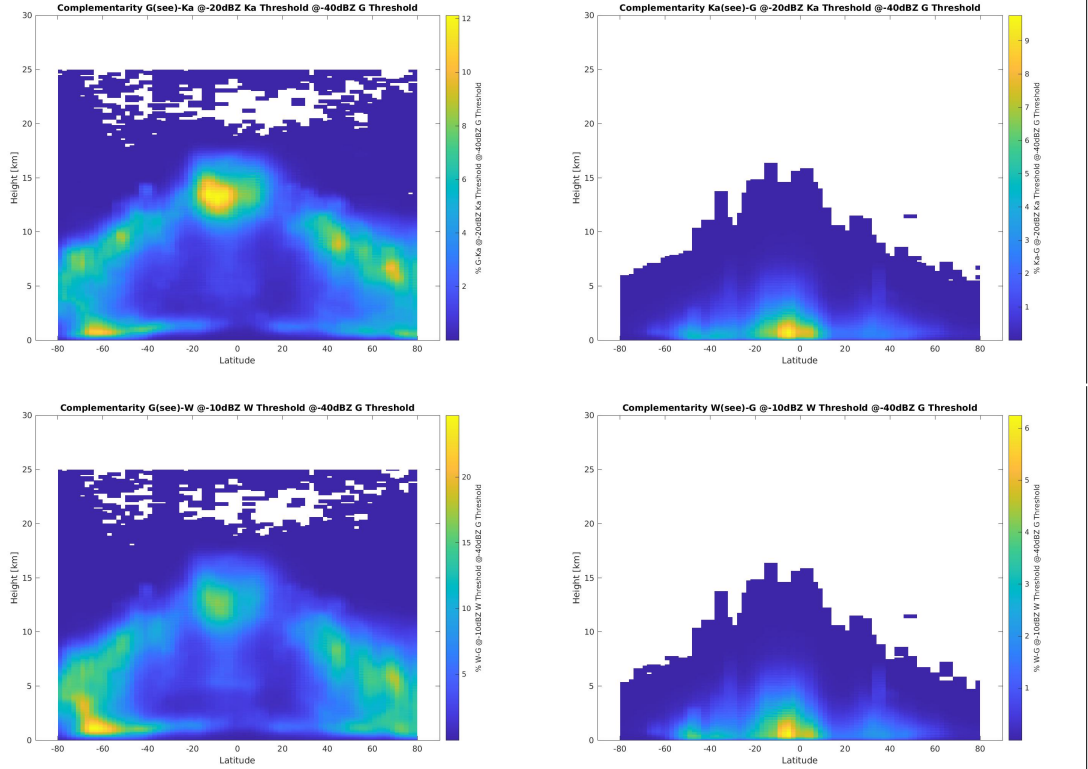


Figure 3.5: Statistical complementary detection percentage in a zonal plot of G-Ka (top left) with -20dBZ and -40dBZ sensitivity threshold and G-W (bottom left) with -30dBZ and -20dBZ sensitivity threshold synergy. On the right column the counterparts of complementarity: Ka-G (top left) and W-G (bottom right). First one in the frequency pair detect and the other don't. Notice that color scales differ from panel to panel.

As expected optimal complementarity stands in low latitude regions (see Fig. 3.5), depending on what frequency system is detecting and what isn't. In fact G-band is detecting and Ka band isn't at all latitudes and high altitudes, thus the frequency pair is complementary thanks to the ability of G-band of detecting smaller hydrometeor particles. On the other hand when Ka detect and G doesn't the best region is low altitude around the equator where most of the annual precipitation

occurs.

3.4 Surface detection analysis

The surface return strength is generally related to the atmospheric attenuation of the signal and to the surface normalised backscattering cross section (σ_0 , A. Battaglia, Wolde, et al. 2017). Since the latter can be estimated via geophysical models, particularly over ocean, then from the surface dimming the PIA can be directly inferred (this is known as surface reference technique, Meneghini and Kozi 1990; Meneghini, Kim, et al. 2015). In order to apply such a technique the surface needs to produce a signal which is higher than the sensitivity of the radar but, in presence of large equivalent water paths (WP), the PIA can drive the signal below the sensitivity threshold. Since the PIA will have different probability density function at the different latitudes it is important to assess how frequently the surface can be actually detected for the different radar systems.

Figure Fig. 3.6 shows that the G band surface detection is very dependant on sensitivity threshold, thus on the technology used, where a 0dBZ sensitive G-band radar would suffer heavily from attenuation on mid-low latitudes peaking the minimum at 10% of surface detection. If the sensitivity is lowered to -20 dBZ then the minimum surface detection probability is increased to 60%; the high end counterpart at -40 dBZ of sensitivity introduce a further improvement of 10% in low latitude region, suggesting that attenuation that cause this additional improvement in surface detection is related to heavy precipitation events. On the other hand the low end sensitivity G-band radar (0 dBZ) would be impaired in the detection from clouds and regular precipitations.

Seen that differences in surface detection at different sensitivity threshold for lower frequencies (Ka and W) are negligible, synergistic or complementary studies on surface detection are equal to the results of single frequency G-band studies (fig.3.7). The only contribute in surface detection comes from G-band and varying its sensitivity threshold has a big impact in function of the latitude.

3.4. SURFACE DETECTION ANALYSIS

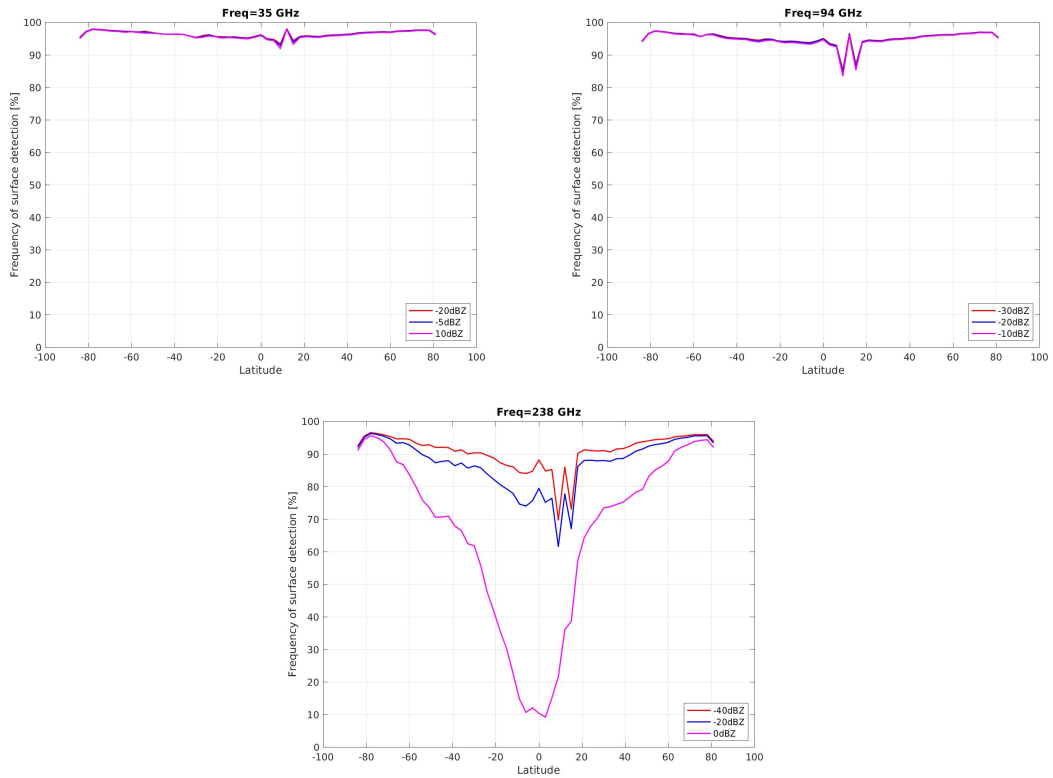


Figure 3.6: Ka-band (top left), W-band (top right) and G-band (bottom) surface detection. Lower frequencies (Ka and W) experience low levels of attenuation, hence sensitivity thresholds does not affect surface detection.

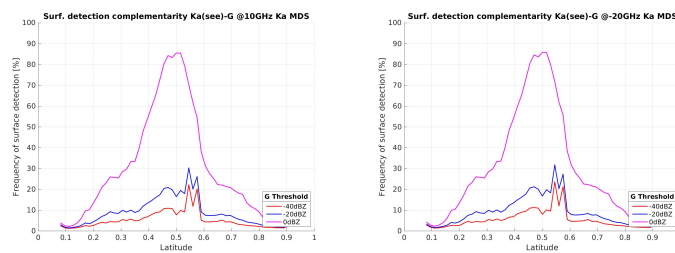


Figure 3.7: Surface detection complementarity Ka-G with different Ka thresholds 10dBZ(left) and -20dBZ (right) surface detection and different G-band thresholds 0dBZ (magenta) -20dBZ (blue) -40dBZ (red). Same levels are reached by all the different Ka-band sensitivity thresholds.

Chapter 4

Super Cooled Liquid Water Cloud insertion effects to a profile retrieval

In this last chapter a super cooled liquid water cloud will be artificially inserted in an existing CloudSat scene to simulate what difference there would be in the retrieval of radar products. Selected scene is located in south Atlantic Ocean with icy clouds and icy precipitation only to simulate the best case scenario of detection of a SCLWC by G-band, seen that in any other environment with liquid precipitation or in water vapour rich clouds results would be very dim resulting in difficulty to detect SCLWC.

This is caused by the high amount of attenuation that water vapour rich clouds with liquid precipitation produce compared to icy clouds. In both the cases clouds were added at iso-Temperature of 245K spanning roughly $1^\circ/2^\circ$ of latitude and 250m of altitude, its water content ($1.04 \frac{g}{m^3}$) is set to produce a total water path addition of $0.25 \frac{kg}{m^2}$ visible in fig.4.1. The intent of this cloud insertion is to quantify the differential reflectivity and to have measurable data of differential attenuation generated by the same scene, one modified and one original without the SCLWC. Results suggest that G-band will produce higher differentials, thus measurable products to characterize a potential SCLWC with

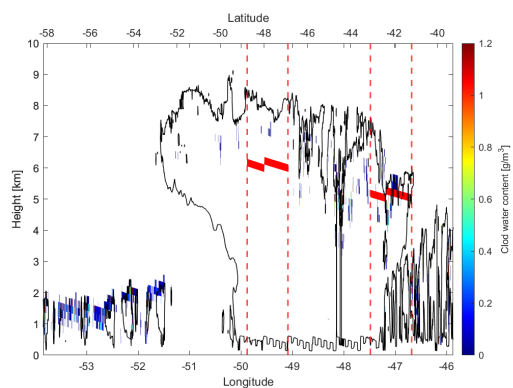


Figure 4.1: Example of two SCLWC insertion in an Atlantic system

real data.

4.1 SCLWC insertion in south Atlantic system

The system pictured in fig.4.2 is located east offshore of Falkland islands:

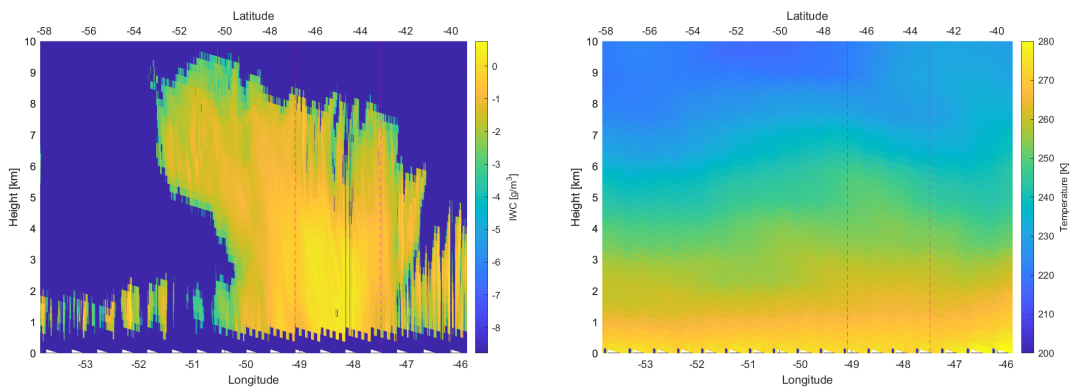


Figure 4.2: Atlantic system Ice water content (left) and Temperature (right). Red dotted lines indicate one of the bounds where the clouds were inserted

The profile that will be studied is the one inserted at coordinates: $-47^{\circ}; -49^{\circ}$, in figure Fig.4.1 can be seen the position of added clouds roughly at 6km of altitude in the core of the ice cloud.

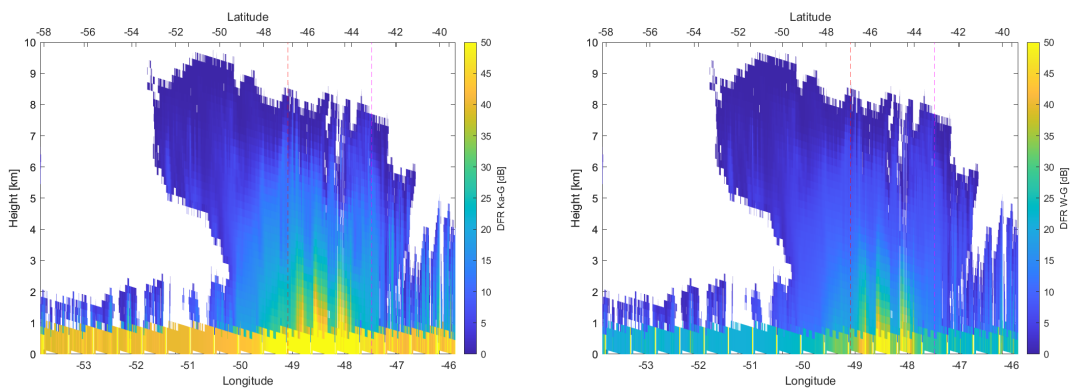


Figure 4.3: Atlantic system DFR Ka-G(left) and W-G (right). Pay attention at the different color scales

In figure Fig.4.3 there is for reference the reflectivity profile in Ka and G-band of the event, it is useful to compare fig.4.4 DFR levels of pre-insertion minus post-insertion with single frequency measurements; Results shows that this cloud

4.1. SCLWC INSERTION IN SOUTH ATLANTIC SYSTEM

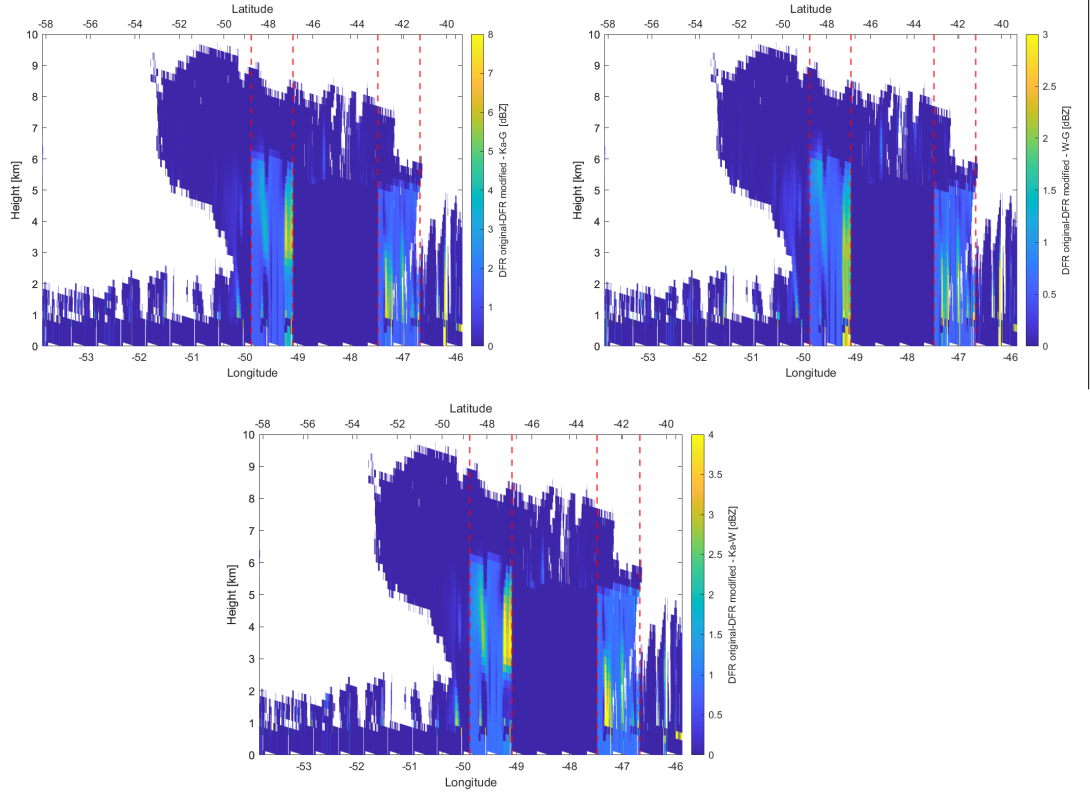


Figure 4.4: Atlantic system differential reflectivity (post insertion minus pre insertion) Ka-G (left) and W-G (right). Red dotted lines indicate one of the bounds where the clouds were inserted. Pay attention that color scales differs from one another.

insertion generates measurable levels of differential on average of 3 dB in Ka-G band pair and less measurable ones in the Ka-W and W-G band pairs in the order of fraction of a decibel. G-band has an obvious advantage it could be used in pair with Ka-band to investigate the existence of SCLWC in icy systems with a good return in terms of additional attenuation that G experience. 1 dB of difference in a cloud with a profile that generates 10/15 dBZ is not measurable, in the case of W-G return, but in contrast Ka-G pair generates 3dB a more noticeable effect.

Varying the temperature, thus the altitude, at which the cloud is inserted does not change the end result of this study because the effect of the temperature on the attenuation is less noticeable than a change in water content. The detectability and the differential signal would be the same but the cloud would change for sure its heat radiative behaviour as the temperature change.

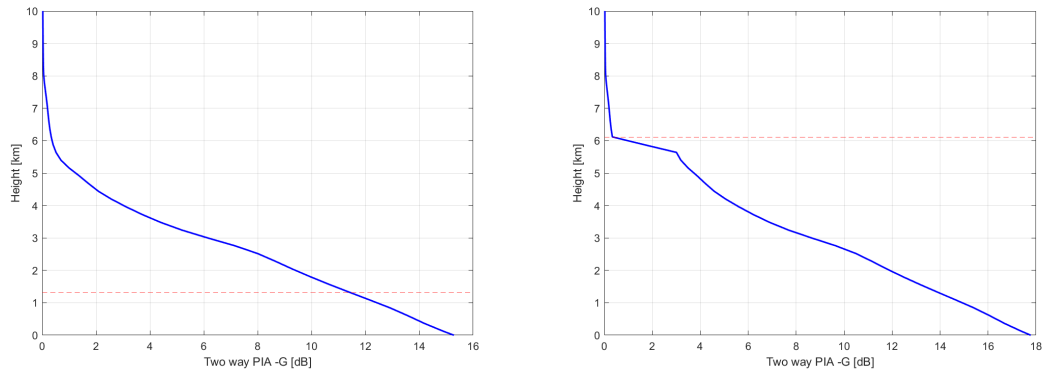


Figure 4.5: Atlantic system profile at coordinates $(-47^{\circ};-49^{\circ})$ 2 way G-band attenuation Original (left) and SCLWC inserted (right).

Chapter 5

Conclusions

Past (TRMM and CloudSat) and present spaceborne based radar missions (GPM and RainCube) has contributed to current knowledge of atmospheric events, but important observation gaps still remain for an in depth understanding of the water cycle and its evolution in a warming climate.

Advancements in Schottky diode technology, frequency-multiplication-based sources, and frequency-modulated, continuous-wave radars led G-band radar systems to higher Technology Readiness Levels (TRLs), enhancing power and sensitivity to levels that meet the requirements to address the challenge. In addition space-borne platforms offer a clear vantage point for the observations of clouds in the ice phase compared to their ground-based counterpart because most of the attenuation is caused by water vapor and hydrometeors in liquid phase which are mainly found in the lower troposphere. All of the above considerations suggest that a space-borne mission including a G-band payload targeted at the study of ice clouds and polar regions is now becoming more and more mature. In fact all major space agencies (ESA, NASA and JAXA) are now considering G-band observation capabilities as part of future satellites for cloud and precipitation remote sensing.

This thesis fits in this framework by investigating the potential of a G-band system embarked in either a smaller platform like those foreseen for the ESA SCOUT or a more complex one as envisaged for an Earth Explorer like mission.

Single frequency analysis on case studies of ice clouds with precipitation at high, mid and low latitudes illustrates the strong potential of G-band radars; high latitudes events are the perfect application case thanks to the minimum attenuation experienced, the increased detection of clouds with smaller water contents and the characterization of ice crystals with sub-millimeter size well beyond the limits (1-2 mm) achievable with current touchstone Ka and W band pair.

Dual frequency pairs advantages have been investigated in the range Ka-W band with G band (35 GHz for Ka, 94 GHz for W and 238 GHz for G-band) over single

frequency systems. The steep DWR Ka–G dynamic range gradients in Fig. 1.8 suggests that DFR Ka–G signals are more sensitive to changes in particle dimensions, hence allowing for more accurate retrievals compared to those achievable using a Ka–W pair.

The effectiveness of complementary and synergistic approaches has been quantified by a statistical analysis based on zonal plots (x-axis: latitude; y-axis: altitude), thus highlighting the cloud regimes (and thus the associated science topics) that are optimally targeted by dual-frequency radar observations. Results shows that complementarity between a low-high frequency pair can be achieved enabling a more complete understanding of mid-latitude events, characterized by the presence of mixed-phase (liquid and solid) layers. This co-presence of different phases on the same layer necessitates a multi-frequency approach to be fully pictured due to the high variability range of hydrometeor size, phase and water content. Thus low altitude precipitation, cloud tops and ice precipitation could be fully characterized at the same time thanks to the complementarity of the different frequencies. Synergy, on the other hand, is more complicated, being dependant on where both signals has enough return and small/moderate amount of attenuation in order to avoid regions of strong attenuation that are difficult to interpret (A. Battaglia, Mroz, et al. 2016; A. Battaglia, Tanelli, et al. 2020); regions that satisfy these constraints are bridge shaped in the zonal plots depicted in Fig. 3.4, clustered always above the melting layer and well below cloud tops in order to allow lower frequencies a measurable return.

SCLWC simulations suggest that the presence of a SCLWC layer inside an ice cloud system could be detected with a small but appreciable signal of several dB depending on the liquid water path with a two-way differential signal Ka-G of about 2.4 dB per 100 g/m². The identification and quantification of the total liquid water path in SLWC has massive implications for the radiative balance of the atmosphere. A thorough understanding of such type of clouds can lead to a considerable reduction in the uncertainties of the projections of global warming in current climate models.

Future developments could include:

1. the expansion of the dataset used for the statistical analysis to make the results more robust;
2. the development of a retrieval algorithm for the microphysical (water contents, characteristic sizes) and macrophysical (thickness, cloud boundaries) properties of ice and SLWC clouds;
3. the study of the impact of the inclusion of radiometric channels in the radar systems (A. Battaglia and Panegrossi 2020).

Bibliography

- [1] *WCRP Grand Challenges*. <http://wcrp-climate.org/grand-challenges>. 2022 (cit. on p. 1).
- [2] Intergovernmental Panel on Climate Change. *Climate Change 2023 Synthesis Report*. 2023 (cit. on p. 1).
- [3] Alessandro Battaglia et al. «Spaceborne Cloud and Precipitation Radars: Status, Challenges, and Ways Forward». In: *Reviews of Geophysics* 58.3 (2020). e2019RG000686 10.1029/2019RG000686, e2019RG000686. DOI: <https://doi.org/10.1029/2019RG000686>. eprint: <https://agupubs.onlinelibrary.wiley.com/doi/pdf/10.1029/2019RG000686>. URL: <https://agupubs.onlinelibrary.wiley.com/doi/abs/10.1029/2019RG000686> (cit. on pp. 1, 10).
- [4] Wanda Szyrmer, Aleksandra Tatarevic, and Pavlos Kollias. «Ice clouds microphysical retrieval using 94-GHz Doppler radar observations: Basic relations within the retrieval framework». In: *Journal of Geophysical Research: Atmospheres* 117.D14 (2012). DOI: <https://doi.org/10.1029/2011JD016675> (cit. on p. 1).
- [5] Gail M. Skofronick-Jackson, Benjamin T. Johnson, and S. Joseph Munchak. «Detection Thresholds of Falling Snow From Satellite-Borne Active and Passive Sensors». In: *IEEE Transactions on Geoscience and Remote Sensing* 51.7 (2013). DOI: 10.1109/TGRS.2012.2227763 (cit. on p. 1).
- [6] Matthew W. Christensen, Graeme L. Stephens, and Matthew D. Lebsock. «Exposing biases in retrieved low cloud properties from CloudSat: A guide for evaluating observations and climate data». In: *Journal of Geophysical Research: Atmospheres* 118.21 (2013). DOI: <https://doi.org/10.1002/2013JD020224> (cit. on p. 2).
- [7] Dongyang Liu, Qi Liu, Guosheng Liu, Junbo Wei, Shumei Deng, and Yunfei Fu. «Multiple Factors Explaining the Deficiency of Cloud Profiling Radar on Detecting Oceanic Warm Clouds». In: *Journal of Geophysical Research: Atmospheres* 123.15 (2018). DOI: <https://doi.org/10.1029/2017JD028053> (cit. on p. 2).

- [8] P. Kollias, E. E. Clothiaux, M. A. Miller, B. A. Albrecht, G. L. Stephens, and T. P. Ackerman. «Millimeter-Wavelength Radars: New Frontier in Atmospheric Cloud and Precipitation Research». In: *Bulletin of the American Meteorological Society* 88.10 (2007). DOI: 10.1175/BAMS-88-10-1608 (cit. on p. 2).
- [9] Graeme L. Stephens et al. «THE CLOUDSAT MISSION AND THE A-TRAIN». In: *Bulletin of the American Meteorological Society* 83.12 (2002). DOI: 10.1175/BAMS-83-12-1771 (cit. on p. 2).
- [10] Graeme Stephens, David Winker, Jacques Pelon, Charles Trepte, Deborah Vane, Cheryl Yuhas, Tristan LÉcuyer, and Matthew Lebsock. «CloudSat and CALIPSO within the A-Train: Ten Years of Actively Observing the Earth System». In: *Bull. Amer. Met. Soc.* 99.3 (2018). DOI: 10.1175/BAMS-D-16-0324.1 (cit. on p. 2).
- [11] S. Tanelli, S. L. Durden, E. Im, K. S. Pak, D. G. Reinke, P. Partain, J. M. Haynes, and R. T. Marchand. «CloudSat’s Cloud Profiling Radar After Two Years in Orbit: Performance, Calibration, and Processing». In: *IEEE Trans. Geosci. Remote Sens.* 46.11 (2008). ISSN: 1558-0644. DOI: 10.1109/TGRS.2008.2002030 (cit. on pp. 3, 19).
- [12] David M. Winker, Mark A. Vaughan, Ali Omar, Yongxiang Hu, Kathleen A. Powell, Zhaoyan Liu, William H. Hunt, and Stuart A. Young. «Overview of the CALIPSO Mission and CALIOP Data Processing Algorithms». In: *Journal of Atmospheric and Oceanic Technology* 26.11 (2009). DOI: 10.1175/2009JTECHA1281.1 (cit. on p. 3).
- [13] A. J. Illingworth et al. «The EarthCARE Satellite: The Next Step Forward in Global Measurements of Clouds, Aerosols, Precipitation, and Radiation». In: *Bull. Amer. Met. Soc.* 96.8 (2015), pp. 1311–1332. DOI: 10.1175/BAMS-D-12-00227.1. eprint: <https://doi.org/10.1175/BAMS-D-12-00227.1>. URL: <https://doi.org/10.1175/BAMS-D-12-00227.1> (cit. on p. 3).
- [14] K. Lamer, P. Kollias, A. Battaglia, and S. Preval. «Mind the gap – Part 1: Accurately locating warm marine boundary layer clouds and precipitation using spaceborne radars». In: *Atm. Meas. Tech.* 13.5 (2020). DOI: 10.5194/amt-13-2363-2020 (cit. on p. 3).
- [15] A. Battaglia, P. Kollias, R. Dhillon, K. Lamer, M. Khairoutdinov, and D. Watters. «Mind the gap – Part 2: Improving quantitative estimates of cloud and rain water path in oceanic warm rain using spaceborne radars». In: *Atm. Meas. Tech.* 13.9 (2020). DOI: 10.5194/amt-13-4865-2020 (cit. on p. 3).

- [16] Pavlos Kollias, Alessandro Battaglia, Katia Lamer, Bernat Puigdomenech Treserras, and Scott A. Braun. «Mind the Gap - Part 3: Doppler Velocity Measurements From Space». In: *Frontiers in Remote Sensing* 3 (2022). ISSN: 2673-6187. DOI: 10.3389/frsen.2022.860284 (cit. on p. 3).
- [17] S. Tanelli, Z. Haddad, E. Im, S. Durden, O. Sy, E. Peral, G. Sadowy, and M. Sanchez-Barbety. «Radar concepts for the next generation of spaceborne observations of cloud and precipitation processes». In: *IEEE Proceedings of Radar Conference, Oklahoma City, OK*. 2018 (cit. on p. 3).
- [18] Graeme Stephens, Antony Freeman, et al. «The Emerging Technological Revolution in Earth Observations». In: *Bull. Amer. Met. Soc.* 101.3 (2020). DOI: 10.1175/BAMS-D-19-0146.1 (cit. on p. 3).
- [19] Frédéric Tridon, Alessandro Battaglia, and Pavlos Kollias. «Disentangling Mie and attenuation effects in rain using a Ka-W dual-wavelength Doppler spectral ratio technique». In: *Geophys. Res. Lett.* 40.20 (2013). DOI: 10.1002/2013GL057454 (cit. on p. 3).
- [20] F. Tridon and A. Battaglia. «Dual-frequency radar Doppler spectral retrieval of rain drop size distributions and entangled dynamics variables». In: *J. Geophys. Res. Atm.* 120.11 (2015). DOI: 10.1002/2014JD023023 (cit. on p. 3).
- [21] Frederic Tridon, Alessandro Battaglia, and Daniel Watters. «Evaporation in action sensed by multiwavelength Doppler radars». In: *J. Geophys. Res. Atm.* 122.17 (2017). DOI: 10.1002/2016JD025998 (cit. on p. 3).
- [22] F. Tridon, A. Battaglia, E. Luke, and P. Kollias. «Rain retrieval from dual-frequency radar Doppler spectra: validation and potential for a midlatitude precipitating case-study». In: *Quart. J. Roy. Meteor. Soc.* 143.704 (2017). DOI: 10.1002/qj.3010 (cit. on p. 3).
- [23] A. Battaglia, S. Tanelli, F. Tridon, S. Kneifel, J. Leinonen, and P. Kollias. «Satellite precipitation measurement». In: vol. 1. *Adv. Global Change Res.* ISBN: 978-3-030-24567-2. Springer, 2020. Chap. Triple-frequency radar retrievals (cit. on pp. 3, 45).
- [24] F. Tridon, A. Battaglia, and S. Kneifel. «Estimating total attenuation using Rayleigh targets at cloud top: applications in multilayer and mixed-phase clouds observed by ground-based multifrequency radars». In: *Atm. Meas. Tech.* 13.9 (2020). DOI: 10.5194/amt-13-5065-2020 (cit. on p. 3).
- [25] Stefan Kneifel, Annakaisa von Lerber, Jussi Tiira, Dmitri Moisseev, Pavlos Kollias, and Jussi Leinonen. «Observed relations between snowfall microphysics and triple-frequency radar measurements». In: *Journal of Geophysical Research: Atmospheres* 120.12 (2015). DOI: <https://doi.org/10.1002/2015JD023156> (cit. on p. 3).

- [26] S. Kneifel, P. Kollias, A. Battaglia, J. Leinonen, M. Maahn, H. Kalesse, and F. Tridon. «First observations of triple-frequency radar Doppler spectra in snowfall: Interpretation and applications». In: *Geophys. Res. Lett.* 43.5 (2016). DOI: 10.1002/2015GL067618 (cit. on p. 3).
- [27] Frédéric Tridon, Alessandro Battaglia, Randy J. Chase, et al. «The Microphysics of Stratiform Precipitation During OLYMPEX: Compatibility Between Triple-Frequency Radar and Airborne In Situ Observations». In: *J. Geophys. Res. Atm.* 124.15 (2019). DOI: 10.1029/2018JD029858 (cit. on p. 3).
- [28] K. Mroz, A. Battaglia, C. Nguyen, A. Heymsfield, A. Protat, and M. Wolde. «Triple-frequency radar retrieval of microphysical properties of snow». In: *Atm. Meas. Tech.* 14.11 (2021). DOI: 10.5194/amt-14-7243-2021 (cit. on p. 3).
- [29] C. M. Nguyen, M. Wolde, A. Battaglia, L. Nichman, N. Bliankinshtein, S. Haimov, K. Bala, and D. Schuettmeyer. «Coincident in situ and triple-frequency radar airborne observations in the Arctic». In: *Atm. Meas. Tech.* 15.3 (2022). DOI: 10.5194/amt-15-775-2022 (cit. on p. 3).
- [30] F. Tridon, I. Silber, A. Battaglia, S. Kneifel, A. Fridlind, P. Kalogeras, and R. Dhillon. «Highly supercooled riming and unusual triple-frequency radar signatures over McMurdo Station, Antarctica». In: *Atmospheric Chemistry and Physics* 22.18 (2022). DOI: 10.5194/acp-22-12467-2022 (cit. on p. 3).
- [31] A. Battaglia, C. D. Westbrook, S. Kneifel, P. Kollias, N. Humpage, U. Löhnert, J. Tyynelä, and G. W. Petty. «G band atmospheric radars: new frontiers in cloud physics». In: *Atm. Meas. Tech.* 7.6 (2014), pp. 1527–1546. DOI: 10.5194/amt-7-1527-2014. URL: <https://www.atmos-meas-tech.net/7/1527/2014/> (cit. on p. 3).
- [32] Katia Lamer, Mariko Oue, Alessandro Battaglia, Richard Roy, Ken Cooper, Ranvir Dhillon, and Pavlos Kollias. «First Light Multi-Frequency Observations with a G-band radar». In: *Atmospheric Measurement Techniques Discussions* (2020). ISSN: 1867-1381. DOI: 10.5194/amt-2020-493 (cit. on p. 3).
- [33] Benjamin M. Courtier et al. «First Observations of G-Band Radar Doppler Spectra». In: *Geophysical Research Letters* 49.4 (2022). ISSN: 19448007. DOI: 10.1029/2021GL096475 (cit. on p. 3).
- [34] B. M. Courtier, A. Battaglia, and K. Mroz. «Advantages of G-band radar in multi-frequency, liquid phase microphysical retrievals». In: *EGUsphere* 2024 (2024). DOI: 10.5194/egusphere-2024-205 (cit. on p. 3).

- [35] Juan M Socuellamos, Raquel Rodriguez Monje, Matthew D Lebsock, Ken B Cooper, Robert M Beauchamp, Arturo Umeyama, and Raquel Rodriguez Monje. «Multifrequency radar observations of marine clouds during the EPCAPE campaign». In: *Earth System Science Data Discussions* (2024). DOI: 10.5281/zenodo.10076228 (cit. on p. 3).
- [36] S. L. Mason, R. J. Hogan, A. Bozzo, and N. L. Pounder. «A unified synergistic retrieval of clouds, aerosols and precipitation from EarthCARE: the ACM-CAP product». In: *EGUsphere* 2022 (2022). DOI: 10.5194/egusphere-2022-1195 (cit. on pp. 4, 19).
- [37] *Extinction*. John Wiley and Sons, Ltd, 1983. ISBN: 9783527618156. DOI: <https://doi.org/10.1002/9783527618156.ch11> (cit. on p. 8).
- [38] Roger Lhermitte. «Attenuation and Scattering of Millimeter Wavelength Radiation by Clouds and Precipitation». In: *Journal of Atmospheric and Oceanic Technology* 7.3 (1990). DOI: 10.1175/1520-0426(1990)007<0464:AASOMW>2.0.CO;2 (cit. on p. 9).
- [39] Robin J. Hogan and Christopher D. Westbrook. «Equation for the Microwave Backscatter Cross Section of Aggregate Snowflakes Using the Self-Similar Rayleigh–Gans Approximation». In: *Journal of the Atmospheric Sciences* 71.9 (2014). DOI: 10.1175/JAS-D-13-0347.1 (cit. on p. 17).
- [40] Robin J. Hogan, Ryan Honeyager, Jani Tyynelä, and Stefan Kneifel. «Calculating the millimetre-wave scattering phase function of snowflakes using the self-similar Rayleigh–Gans Approximation». In: *Quarterly Journal of the Royal Meteorological Society* 143.703 (). DOI: <https://doi.org/10.1002/qj.2968> (cit. on p. 17).
- [41] Jussi Leinonen, Stefan Kneifel, and Robin J. Hogan. «Evaluation of the Rayleigh–Gans approximation for microwave scattering by rimed snowflakes». In: *Quarterly Journal of the Royal Meteorological Society* 144.S1 (). DOI: <https://doi.org/10.1002/qj.3093> (cit. on p. 17).
- [42] U Baltensperger, M Schwikowski, D.T Jost, S Nyeki, H.W Gäggeler, and O Poulida. «Scavenging of atmospheric constituents in mixed phase clouds at the high-alpine site jungfraujoeh part I: Basic concept and aerosol scavenging by clouds». In: *Atmospheric Environment* 32.23 (1998). ISSN: 1352-2310. DOI: [https://doi.org/10.1016/S1352-2310\(98\)00051-X](https://doi.org/10.1016/S1352-2310(98)00051-X) (cit. on p. 17).
- [43] S. S. Lee. «Dependence of aerosol-precipitation interactions on humidity in a multiple-cloud system». In: *Atmospheric Chemistry and Physics* 11.5 (2011). DOI: 10.5194/acp-11-2179-2011 (cit. on p. 17).

- [44] B. Dolan, B. Fuchs, S. A. Rutledge, E. A. Barnes, and E. J. Thompson. «Primary Modes of Global Drop Size Distributions». In: *Journal of the Atmospheric Sciences* 75.5 (2018). DOI: 10.1175/JAS-D-17-0242.1 (cit. on p. 23).
- [45] RAL space G band project team. «G-Band Spaceborne Radar Instrument for Atmospheric Missions Technology Roadmap, Conclusions and Perspectives». In: (2024) (cit. on p. 24).
- [46] Alison M. Anders and Stephen W. Nesbitt. «Altitudinal Precipitation Gradients in the Tropics from Tropical Rainfall Measuring Mission (TRMM) Precipitation Radar». In: *Journal of Hydrometeorology* 16.1 (2015). DOI: 10.1175/JHM-D-14-0178.1 (cit. on p. 28).
- [47] A. Battaglia, M. Wolde, L. P. D’Adderio, C. Nguyen, F. Fois, A. Illingworth, and R. Midthassel. «Characterization of Surface Radar Cross Sections at W-Band at Moderate Incidence Angles». In: *IEEE Trans. Geosci. Remote Sens.* 55.7 (2017). 10.1109/TGRS.2017.2682423, pp. 3846–3859 (cit. on p. 38).
- [48] Robert Meneghini and Toshiaki Kozu. *Spaceborne weather radar*. Artech House, 1990 (cit. on p. 38).
- [49] Robert Meneghini, Hyokyung Kim, Liang Liao, Jeffrey A. Jones, and John M. Kwiattkowski. «An Initial Assessment of the Surface Reference Technique Applied to Data from the Dual-Frequency Precipitation Radar (DPR) on the GPM Satellite». In: *J. Atmos. Ocean. Tech.* 32.12 (2015). DOI: <http://dx.doi.org/10.1175/JTECH-D-15-0044.1> (cit. on p. 38).
- [50] A. Battaglia, K. Mroz, Tim Lang, F. Tridon, S. Tanelli, Lin Tian, and Gerald M. Heymsfield. «Using a multiwavelength suite of microwave instruments to investigate the microphysical structure of deep convective cores». In: *J. Geophys. Res. Atm.* 121.16 (2016), pp. 9356–9381. DOI: 10.1002/2016JD025269. eprint: <https://agupubs.onlinelibrary.wiley.com/doi/pdf/10.1002/2016JD025269>. URL: <https://agupubs.onlinelibrary.wiley.com/doi/abs/10.1002/2016JD025269> (cit. on p. 45).
- [51] A. Battaglia and G. Panegrossi. «What Can We Learn from the CloudSat Radiometric Mode Observations of Snowfall over the Ice-Free Ocean?» In: *Radio Sci.* 12.20 (2020). ISSN: 2072-4292. DOI: 10.3390/rs12203285. URL: <https://www.mdpi.com/2072-4292/12/20/3285> (cit. on p. 45).